

The effects of annealing treatment on mechanical properties of nanocrystalline α -iron:
an atomistic study

by

Xuhang Tong

A thesis submitted in partial fulfillment of the requirements for the degree of

Master of Science

in

Materials Engineering

Department of Chemical and Materials Engineering
University of Alberta

© Xuhang Tong, 2015

Abstract

Nanocrystalline metallic materials demonstrate superior mechanical, optical, and electric properties. Claims are often found in the literature that metallic materials can be nanocrystallized by severe plastic deformation (SPD). However, SPD does not generate a well-defined nanocrystalline material, which can be achieved by subsequent annealing/recovery treatment. In this study, molecular dynamics simulation is employed to investigate 1) the role of grain boundaries during deformation processes of nanocrystalline α -iron; 2) intrinsic effects of annealing treatment on mechanical properties of nanocrystalline α -iron. Investigations of the structures and deformation behaviors have demonstrated that local structure and local stress at grain boundary areas determine the overall mechanical properties of nanocrystalline. To simulate nanocrystalline α -iron generated by SPD process, we built a polycrystalline system and applied cyclic load to the system to generate abundant internal defects. The simulation demonstrates that grain boundary in the deformed NC α -iron evolve to a more equilibrium state, eliminating or minimizing the residual stress during annealing treatment. The annealing treatment increases the system's strength by reducing dislocation emission sources, and improves materials ductility through strengthening grain boundaries' resistance to intergranular cracks. The results indicate that the annealing treatment is an essential process for obtaining a well-defined NC structure with superior mechanical properties.

Preface

Results presented in Chapter 3 of this thesis have been published as X. Tong, H. Zhang and D.Y. Li, “Effects of misorientation and inclination on mechanical response of $\langle 110 \rangle$ tilt grain boundaries in α -Fe to external stresses”, *Modelling and Simulation in Materials Science and Engineering*, vol. 22, issue 6, 065016(2014).

Results presented in Chapter 4 of this thesis have been published as X. Tong, H. Zhang and D. Y. Li, “Effect of annealing treatment on mechanical properties of nanocrystalline α -iron: an atomistic study”, *Scientific Reports*, vol. 5, 8459 (2015).

For the work in these two papers, I was responsible for building computational models, performing simulations, analyzing data and composing manuscripts. Professor D.Y. Li and Professor H. Zhang contributed to data analysis and manuscripts revisions. All the researches are conducted under Professor D.Y. Li and Professor H. Zhang’s supervisions.

Acknowledgements

I gratefully appreciate Dr. D.Y. Li and Dr. Hao Zhang's guidance and encouragements during my graduate study.

I would like to thank my parents and Miss. Xiaoyu Sun for their supports.

Computational resources provided by WestGrid are appreciated.

Table of Contents

1. Introduction	1
1.1 Nanocrystalline metallic materials	1
1.2 Mechanical properties and deformation mechanism.....	4
1.3 Effects of annealing treatment in NC materials	6
1.4 Grain boundaries in NC materials.....	10
1.5 Objectives of this study.....	14
2. Simulation details	16
2.1 Atomic interaction.....	16
2.2 Model construction.....	19
2.3 Local structure identification	21
2.4 Summary	24
3. Deformation of NC α -iron.....	25
3.1 Simulation configuration.....	25
3.2 Results and discussion.....	30
3.2.1 Energy and volumetric expansion of GBs.....	30
3.2.2 Yield pattern: twinning or dislocation emission.....	32
3.2.3 Yield strength of STGBs	34
3.2.4 Yield strength of ATGBs: local stress analysis.....	38

3.2.5 Comparing the stress distribution of ATGBs and STGBs.....	44
3.3 Summary	46
4. Effects of annealing treatment.....	48
4.1 Simulation details.....	48
4.2 Results.....	51
4.2.1 Voronoi volume and residual stress.....	51
4.2.2 Tensile deformation test	54
4.2.3 Dislocation emission during yielding.....	56
4.2.4 Ductility	58
4.3 Discussion	62
4.4 Summary	64
5. Conclusions	65
5.1 Conclusions.....	65
5.2 Future works.....	66

List of Tables

Table 3.1 Grain boundary tilting angles, plane indices and system size of STGBs and ATGBs bicrystal systems 27

Table 4.1 Mechanical properties of annealed and as-processed systems. σ_{\max} , the maximum stress during tensile deformation; $\sigma_{\text{flow}(\epsilon < 0.2)}$, the flow stress before 20% strain; $\sigma_{\text{flow}(\epsilon > 0.2)}$, the flow stress from 20% strain to failure; $\epsilon_{\text{failure}}$, the plastic strain at failure and K, the toughness..... 56

List of Figures

Figure 1.1 The AFM image of nanocrystallized surface of stainless steel 304[2].....	1
Figure 1.2 Schematics of (a) ECAP and (b) HPT as typical SPD techniques.	2
Figure 1.3 Schematic of surface punching process [7]. The plastic strain applied to surface could breakdown the grain size to nano scale.	3
Figure 1.4 Schematic of strength-grain size dependence from micro scale to nano scale. When the grain size is less than 100 nm, there are deviations from the original Hall-Petch relationship. [13].....	5
Figure 1.5 Strength softening of NC copper at very small grain size.[14] The maximum strength appears around 10 to 15nm. The strength softening under 10nm is due to the dominating role of grain boundary sliding during deformations.	6
Figure 1.6 (a) Stress-strain curves of ARB processed 99.2% Al(curve 1) and ARB and annealing processed Al (curve 2) subjected to tensile test. [4] (b) Micro indentation load-depth curves of stainless steel 304 processed by sandblast and sandblast and annealing.[6] In both cases, annealing treatment increased the strength of NC metals.....	8
Figure 1.7 $\Sigma 11$ coincidence site lattice formed by two FCC grains, the atoms belong to one grain are colored by black while the atoms belong to the other grains are colored by white. [32].....	11
Figure 1.8 Structure units in three symmetric tilted CSL grain boundaries in BCC lattice[39].....	12
Figure 2.1 A bicrystal model employed in this study. Due to the 3D periodic boundary condition, there are two same grain boundaries in the system.	19

Figure 2.2 Voronoi construction is applied to build 3D polycrystalline models in this study. (a) In a $27*27*27 \text{ nm}^3$ cubic box, 27 seeds are randomly placed. (b) A grain with random orientation is generated from a seed. (c) The whole system is generated by Voronoi construction. 20

Figure 2.3 The CNA indices of (a) 441 and (b) 661 in perfect BCC lattice. [55] 22

Figure 2.4 (a) Atomic configuration snapshot of a NC α -iron deformed to 8% strain, atoms are colored by CNA values. (b) Grain boundaries and dislocations information identified by DXA algorithm and plotted by ParaView. Dislocation lines are represented by red lines. 23

Figure 3.1 (a) The schematic of a bicrystal model. There are two identical GBs as periodic boundary conditions applied to all three dimensions. (b) Atomic configuration of a $\Sigma 9$ STGB. Upper crystal and lower crystal are tilted with the same angle but in opposite directions to obtain a symmetric GB structure. (c) Atomic configuration of a $\Sigma 9$ ATGB. The lower grain is fixed and the upper grain is tilted with an angle of 38.94° 26

Figure 3.2 Stress-strain curves for STGB $\Sigma 9$ bicrystal system under tensile deformation with different strain rates using MD simulation. With different strain rates (10^6s^{-1} , 10^7s^{-1} and 10^8s^{-1}), the bicrystal system exhibits the same yielding behavior (twinning emission from GB areas) and the yield strength is about the same (9.16GPa, 9.16GPa and 9.19GPa, respectively). The chosen strain rate, 10^8s^{-1} , could give yield strength data with reasonable accuracy. 29

Figure 3.3 Energy of equilibrium (300K) $\langle 110 \rangle$ symmetric (square) and asymmetric (circle) tilt boundaries with the tilt angle ranging from 20.05° to 90° . For the same

misorientation angle, the GB energy of ATGB is always larger than that of corresponding STGB. The deep cusp occurs at the $\Sigma 3/70.53^\circ$ GBs..... 31

Figure 3.4 Relationship between excess volume and grain boundary energy of STGBs (a) and ATGBs(b). Symmetric $\Sigma 3$ is not included in this plot. 32

Figure 3.5 Generalized stacking fault energy of α -iron [111](112) sliding system. The energy of $a_0/6[111]$ partial dislocation sliding to form a $a_0/3[111]$ partial dislocation ($\Delta\gamma^{slip} = 73\text{mJ/m}^2$) is higher than that for [111](112) twinning ($\Delta\gamma^{twin} = 50\text{mJ/m}^2$), indicating that twinning is a preferred yielding mechanism. 33

Figure 3.6 (a) Stress-strain curves of STGBs bicrystal systems; (b) Yield strengths of $\langle 110 \rangle$ STGBs bicrystal systems with the tilt angle in the range of $20.05^\circ \sim 70.53^\circ$, and that of corresponding single crystal. Yield strengths are also resolved to $\langle 111 \rangle \{112\}$ slip systems, as labeled by square symbols. 36

Figure 3.7 (a) Stress-strain curves of ATGB bicrystal systems. (b) The relation between the GB energy and yield strength. Yield strength is roughly proportional to the GB energy..... 39

Figure 3.8 Stress distribution along a $\Sigma 9$ ATGB in a bicrystal system before yielding. The stress inside the crystals is homogenous, while that at the grain boundary is heterogeneous. The legend is in the unit of GPa. 41

Figure 3.9 (a) In $\Sigma 9$ ATGB bicrystal system, twinning is emitting from grain boundary area into crystal. Only atoms belong to the grain boundary or twin boundary are plotted. (b) Local stress distribution in x- direction of the $\Sigma 9$ ATGB. The local stress varies from 2GPa to 17 GPa. The local stress at the location where twinning emitted is the highest

and so is the Voronoi volume as shown in (c). This verifies that the twinning emission from the grain boundary area is triggered by stress-assisted free volume fluctuation..... 42

Figure 3.10 Overall yield strengths and maximum local stresses versus the tilting angle for different ATGB systems (except $\Sigma 17$ and $\Sigma 43$)..... 43

Figure 3.11 Atomic arrangements of (a) symmetric tilt $\Sigma 3$ grain boundary and (b) asymmetric tilt $\Sigma 3$ grain boundary, after relaxation at 1000K. (c) Stress distribution of $\Sigma 3$ STGB along GB before yielding. (d) Stress distribution along $\Sigma 3$ ATGB before yielding. Green atoms belong to bcc crystals and red atoms belong to GB areas. 45

Figure 4.1 Snapshot of the system configuration (a) and stress-strain curves of cyclic load(b) applied to the system in order to simulate NC α -iron. 49

Figure 4.2 Heat treatment curve of the annealed sample. To anneal the system, the sample are heated to 750 K and kept for 1.6 nanoseconds. 51

Figure 4.3 Cross-section plots of residual stress (σ_{yy}) in (a) as-processed and (b) annealed systems. The plane in Fig.4.1(a) sketched by black lines is the plane of cross-section views displayed in (a) and (b). The pressures in x-, y- and z- directions are 0 bar and the temperature is 300K. Atoms are colored by σ_{yy} ; color map is in unit of GPa. The scale bar is 10nm. Comparisons between (a) and (b) indicate that annealing treatment has reduced the internal stress, driven grain boundaries and triple junctions to more equilibrium states and converted a deformation twinning(region D in (a)) to a $\langle 111 \rangle \{112\}$ edge dislocation(region D' in (b)). 52

Figure 4.4 Statistical distribution of (a) Voronoi volume, (b) hydrostatic pressure and (c) stress tensor in y-direction of each atom in both annealed and as-processed systems.

These histograms quantitatively demonstrate more ordered atomic structures (represented by Voronoi volume) as well as reduced residual stress in the annealed system. 53

Figure 4.5 Stress-strain curves of (a) tensile deformation applied to as-processed sample and annealed sample from no strain to failure, and (b) Enlarged stress-strain curves of an early deformation stage up to 10% strain. 55

Figure 4.6 The cross-section views of (a) as-processed sample and (b) annealed sample at 4.2% strain. Atoms are colored by stress tensor in y- direction (σ_{yy}). Color map is in the unit of GPa. The high local stress of region A in as-processed sample (a) at the strain of 4.2% (a-1) results in emission of a $\frac{1}{2}\langle 111 \rangle$ dislocation at the strain of 4.5% (a-2). At the strain of 4.2%, local stress in the same region in annealed sample (b) is more homogenous, and no dislocation is emitted from this region when deformed further. 57

Figure 4.7 Cross-section views of atomic configurations of the as-processed system during tensile deformation. Atoms are colored by CNA values, while red spheres represent GB and dislocation atoms, green spheres are BCC atoms. As the strain increases, the deformation process includes voids/cracks nucleation, growth and coalescence and eventual failure at 80% strain. The annealed system has the same failure mode of intergranular cracking with the as-processed system. 59

Figure 4.8 Evolution of crack fraction (crack volume/system volume) with tensile strain for annealed and as-processed samples. The inset plot shows details in the early deformation stage with the strain ranged from 0 to 15%. The annealed sample shows a larger resistance to intergranular cracking than as-processed sample. 61

List of Abbreviations

3D	three dimensional
AFM	atomic force microscopy
ARB	accumulative roll bonding
ATGB	asymmetric tilt grain boundary
BCC	body-centered cubic
CNA	common neighbor analysis
CSL	coincidence site lattice
DFT	density function theory
DOF	degree of freedom
DXA	dislocation extraction algorithm
EAM	embedded atom method
ECAP	equal channel angular processing
FCC	face-centered cubic
GB	grain boundary
HAGB	high angle grain boundary
HPT	high pressure torsion
LAGB	low angle grain boundary
L-J	Lennard-Johns
MD	molecular dynamics
NC	nanocrystalline
PBC	periodic boundary condition
SF	Schmid factor
SPD	severe plastic deformation
STGB	symmetric tilt grain boundary
T_m	melt temperature

1. Introduction

1.1 Nanocrystalline metallic materials

In the last few decades, nanocrystalline (NC) metallic materials [1] have drawn wide research interests due to their superior mechanical, optical and electric properties. NC metallic materials with superior strength, toughness and anti-corrosion properties are very promising for a wide variety of applications in industry, including upstream and downstream oil and gas industries. Generally, NC materials are single or multi-phase polycrystalline with nano scale grain size, typically below 250 nm. In NC metallic materials, there are large percentages of atoms belong to grain boundaries or phase boundaries, which may significantly alter the properties in comparison with coarse grained materials with the same compositions. Fig.1.1 shows the Atomic Force Microscopy (AFM) image of surface nanocrystallized stainless steel 304 with average grain size of 31 nm, in which one can observe abundant grain boundaries.

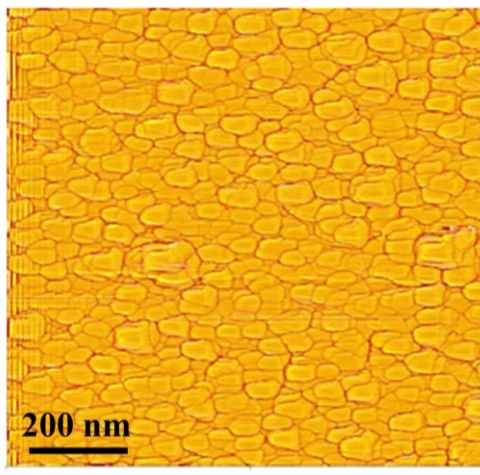


Figure 1.1 The AFM image of nanocrystallized surface of stainless steel 304 [2].

NC materials could be obtained by either consolidating from small particle or breaking down the polycrystalline materials into nanoscale. Specifically, the methods to generate NC materials include inert gas condensation, electrodeposition, crystallization from amorphous materials, severe plastic deformation, *etc.* Among above mention methods, severe plastic deformation (SPD) is a feasible process to generate large-scale NC. The severe plastic strain applied to coarse-grained materials can introduce sufficient defects and break coarse grains into nano grains efficiently.

There are several techniques to apply severe plastic deformations to generate NC materials, *e.g.* equal channel angular processing (ECAP) [3], accumulative roll bonding (ARB) [4], high pressure torsion (HPT) [5] and ball milling. As a typical SPD technique, ECAP (illustrated in Fig.1.2 (a)) uses a die containing two channels with same cross-section and intersecting at an angle. The sample is machined to fit these channels. Large plastic strain can be achieved by pushing the sample through the die. Another sample of SPD technique is high pressure torsion, illustrated in Fig.1.2 (b). In HPT, the sample in the form of plate is held under high pressure and subjected to severe torsion strain.

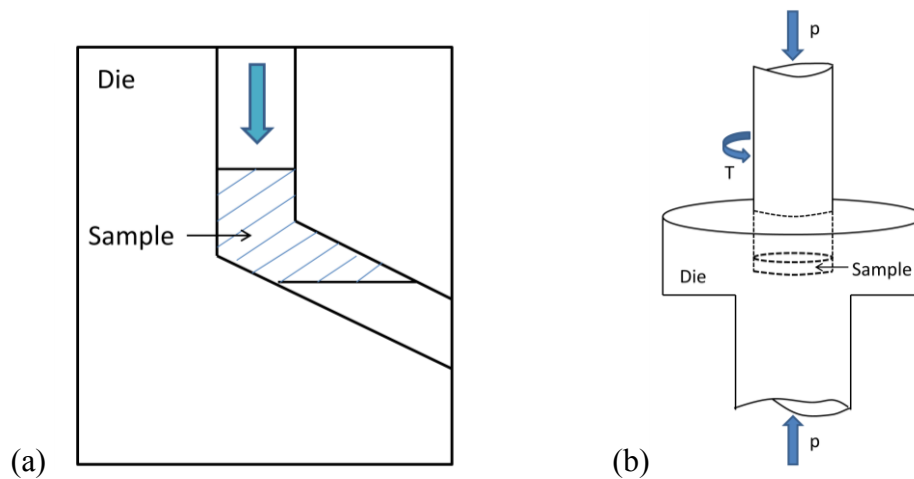


Figure 1.2 Schematics of (a) ECAP and (b) HPT as typical SPD techniques.

SPD techniques are also efficient to nanocrystallize the surface of metallic materials. For instance, sandblasting by silica particles is an effective way to reduce the grain size of metallic materials' surface layers to nano scale [6]. The grain size achieved by sandblasting can reach to 20nm and the thickness of the surface NC layer is about 50 μm [6]. The surface nanocrystallized stainless steel processed by sandblasting and annealing treatment shows 179% higher surface hardness than the conventional coarse-grained materials with the same composition [6]. The superior mechanical properties could significantly improve the wear and corrosion behaviors of stainless steels. Similarly, surface punching process applied to materials surface can also reduce the grain size to nano scale, as the schematic illustrated in Fig.1.3 [7]. These two processes have been successfully applied to nanocrystallized the surface layers of aluminum [8], titanium [9], stainless steel [6] and other alloys [10].

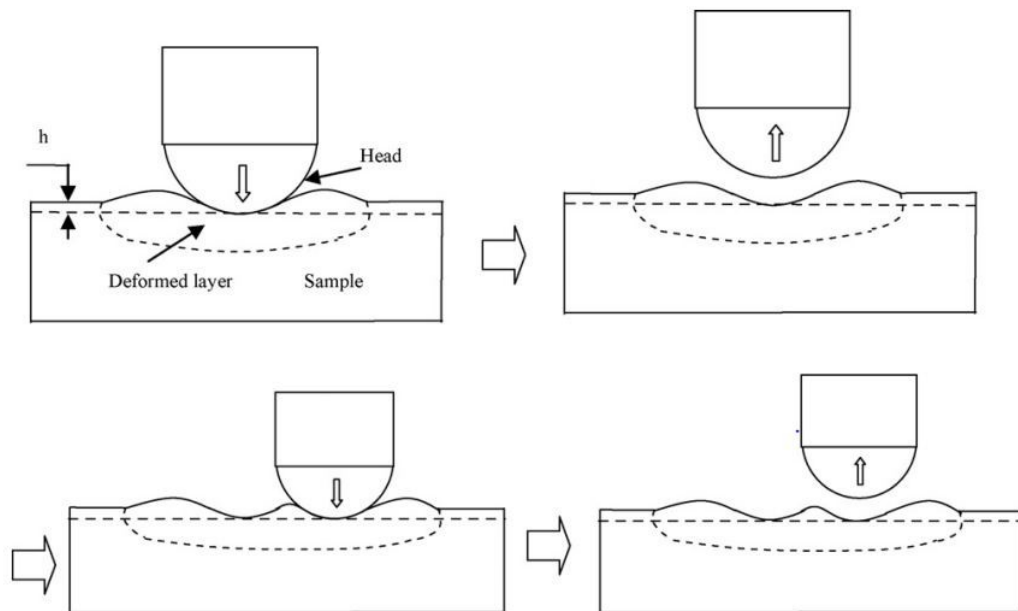


Figure 1.3 Schematic of surface punching process [7]. The plastic strain applied to surface could breakdown the grain size to nano scale.

1.2 Mechanical properties and deformation mechanism

In conventional coarse-grained metals, the strengths are determined by dislocation-dislocation interaction and dislocation-grain boundaries interaction. In coarse-grained materials increased dislocation density could result in higher strength, as more dislocations entangle with each other in this situation. For the dislocation-grain boundaries interaction, *i.e.* dislocation pile-ups at grain boundary areas, there is a well-established equation, Hall-Petch relationship [11] to describe the strength's dependence on grain size (d) :

$$\sigma_y = \sigma_0 + kd^{-n} \quad (1.1)$$

Where σ_y is the yield strength, σ_0 is the friction stress, k is a constant. The parameter n in the power express is usually set to be 0.5, while some time is set other values in the range from 0.3 to 0.7 [12]. According to Hall-Petch relation, one may anticipate increased strength when the grain size of metallic materials reduced to nanoscale, as shown in the left part of Fig.1.4.

Fig.1.4 is an illustration of the dependence of flow stress on grain size from micro scale to nano scale [13]. The left part of Fig.1.4, with the grain size smaller than micro level but larger than 100nm, the strength-grain size relationship matches the Hall-Petch equation. Within this region, the deformation mechanism is still dislocation-grain boundaries interaction, and the strength of the material is determined by the dislocation pile-up at grain boundary areas. However, while the grain size reduced to less than 100 nm, the slope of the $\sigma - d^{1/2}$ curve decrease, and even becomes negative when the grain

size is smaller than 10 nm. This deviation from original Hall-Petch relation is resulted from the transition of deformation mechanisms.

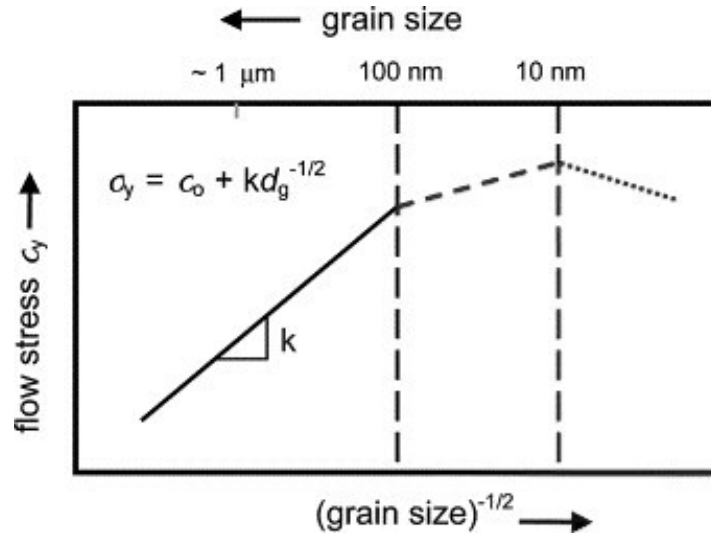


Figure 1.4 Schematic of strength-grain size dependence from micro scale to nano scale. When the grain size is less than 100 nm, there are deviations from the original Hall-Petch relationship [13].

In NC materials with grain size smaller than 100 nm, the dislocation quantities inside single grains are limited. Thus the extent of pile-ups, which is the base of Hall-Petch relation, is limited. The deformation mechanism changed to grain boundaries mediated mechanism, *e.g.* dislocation emission from grain boundaries, grain boundaries sliding, migration and grain rotation. While the grain size down to very small, *i.e.* less than 10nm, softening happens due to the dominating role of grain boundary sliding and grain rotation. Employing large scale molecular dynamics simulation, Schiotez *et al* [14] have demonstrated the deformation mechanism changes to grain boundary sliding when the grain size of NC Cu reduced to 5 nm. Fig.1.5 clearly illustrates the strength softening at very small grain size.

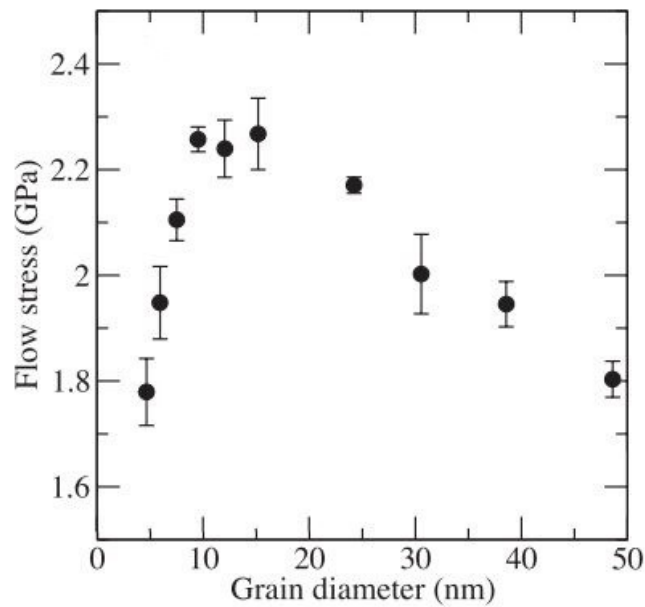


Figure 1.5 Strength softening of NC copper at very small grain size [14]. The maximum strength appears around 10 to 15 nm. The strength softening under 10 nm is due to the dominating role of grain boundary sliding during deformations.

1.3 Effects of annealing treatment in NC materials

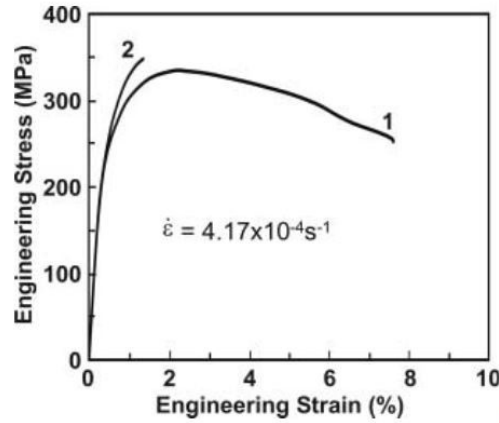
In the structure generated by SPD, nanoscale grain boundaries (GBs), which play very important roles in determining mechanical properties of NC materials, are mostly in non-equilibrium states [15]. Other defects (*e.g.* point defects, twinning, stacking fault and porosity) are also commonly observed in SPD structures. Or in the other words, the grain boundaries produced by SPD are not well defined grain boundaries but boundary between dislocation cells. These non-equilibrium GBs and defects insides grains may significantly influence the mechanical behavior of nanostructures generated by SPD.

To alter the strength and plasticity of NC metallic materials after SPD, subsequent annealing/recovery treatment is applied. In conventional coarse-grained metals, annealing

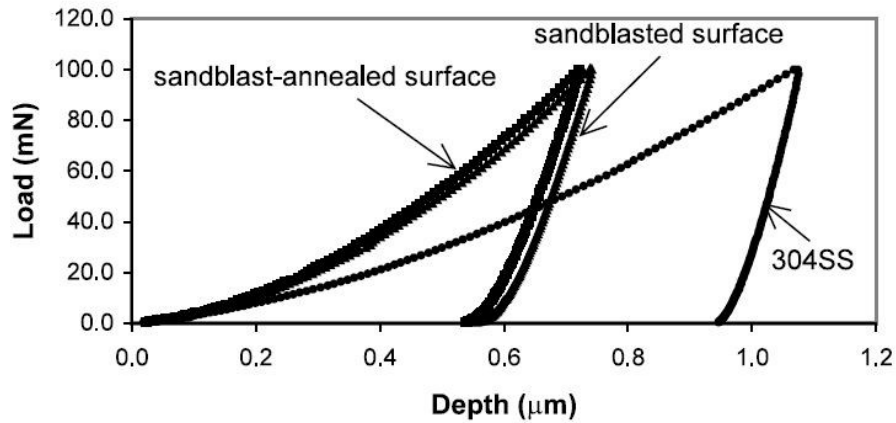
treatment could decrease the strength but increase the plasticity, which is resulted from reduced dislocation density and larger grain size. However, the situation is different in NC metals. Moderate annealing without noticeable grain growth, *i.e.* low temperature and short annealing time, was reported to increase the strength of SPD NC materials [4][16][17]. This phenomenon, termed as “annealing hardening” [4], is opposite to the situations of traditional coarse-grained metals.

During annealing, the grain size stability of NC metallic materials is an important issue. High temperature annealing could easily increase the grain size of NC metals and lose the desired strength. Thus, the parameters of annealing treatment applied to NC metals should be carefully set to avoid undesired grain growth. By carefully tuning the annealing temperature and durations, recovery without noticeable grain growth could be achieved [16][18][19][20]. The annealing treatment in this study refers to above-mentioned moderate annealing treatment without grain growth.

Figure 1.6 (a) shows the engineering stress-strain curves of NC Al samples [4], one was processed by ARB and the other one was processed by ARB and annealing. The strength of annealing processed sample was increased while the plasticity was markedly decreased. In surface nanocrystallized metals, the annealing hardening was also observed. Annealing treatment showed to increase the strength and elastic properties of the surface layer of stainless steel 304, which is nanocrystallized by sandblasting. Figure 1.6 (b) shows the load-depth curve of surface nanocrystallized stainless steel 304, with grain size about 20 nm [6]. In addition, the sandblasted and annealing processed stainless steel sample demonstrated 11% higher hardness than that only processed by sandblasting.



(a)



(b)

Figure 1.6 (a) Stress-strain curves of ARB processed 99.2% Al (curve 1) and ARB and annealing processed Al (curve 2) subjected to tensile test [4]. (b) Micro indentation load-depth curves of stainless steel 304 processed by sandblast and sandblast and annealing [6]. In both cases, annealing treatment increased the strength of NC metals.

Several possible mechanisms are proposed to explain the “annealing hardening” phenomenon. During annealing, the dislocation density decreases, resulting from annihilation of dislocations with opposite Burger’s vectors and dislocation absorption at grain boundaries [21]. On the nanoscale, a system with dislocations starvation may have higher strength [22]. Besides, it has been shown that after annealing, GBs reach more

equilibrium state and become sharper [18]. Sharper GBs are more effective to block dislocations during deformation, thus increase the strength [6]. In NC metals, however, dislocations pile-up is not the main deformation mechanism with limited dislocations inside individual grains. GBs in more equilibrium states raise the barrier to dislocation emission [4][23] and GB sliding [17], corresponding to a higher overall yield strength.

Studies on the effects of annealing on NC metals' ductility reported in literature are however not always consistent. The ductility of NC Ti (with grain size about 120 nm) processed by high pressure torsion was reported to be improved by 30% after annealing at 300°C for 10 min [17]. A similar trend was observed in electrodeposited NC Ni (with grain size about 30 nm) after annealed at 100°C [16]. However, it was also reported that annealing at 150°C markedly lowered the ductility of NC Al (with grain size about 200 nm) produced by ARB [14], which was explained that annealing reduced the dislocation density, so that fewer dislocations were available to conduct plastic deformation.

In the above-mentioned studies, though the materials and annealing parameters are different, the main purpose of performed moderate annealing is the same, *i.e.* to rearrange defects and GBs towards more equilibrium states without grain growth. The inconsistency could be caused by some un-controllable factors, *e.g.* impurity segregation and possible precipitation that may occur during annealing. In ref. [16], the sulfur concentration at grain boundaries in NC Ni could reach up to 6.3 wt. % after annealing, which made the NC Ni exhibit more brittle characteristics. In previous computational studies [24][23], artificially induced non-equilibrium GBs, which are achieved by randomly displacing grain boundary atoms, and relatively small grain size (12 nm, which

is close to the region with inverse Hall-Petch relationship) may complicate the situation with extra factors, such as grain boundary sliding and grain rotation.

These discrepancies indicate that there lacks a thorough understanding about the intrinsic effects of annealing on mechanical properties of NC metals, especially for the less studied BCC metals. Furthermore, the ductility of NC metals, which is represented by the maximum plastic strain at failure during tensile test, can be largely affected by nano cracks/voids nucleation, growth and coalescence [25][26]. The role of fracture was not taken into account in previous studies regarding the effect of annealing on NC metals. To clarify atomic structure changes and intrinsic effects of annealing treatment on mechanical properties of NC metals is the main objective of this study. We choose α -iron as a typical BCC metal due to its widespread industrial applications and well-established database.

1.4 Grain boundaries in NC materials

In NC materials, there is a large percentage of atoms belonging to or affected by grain boundary areas. The abundant grain boundaries in NC materials play crucial roles to determine the materials properties. Dislocations-GBs interactions [27], GB sliding [28], grain rotation [29], GB diffusion [30] and migration [31] all influence mechanical properties of polycrystalline materials. The behavior of GB is strongly affected by its structure and the direction of applied stress. In order to investigate the effects of annealing, it is helpful to study the structure and mechanical behaviors of grain boundaries inside NC α -iron.

Grain boundaries in materials are generally considered to have five degrees of freedoms (DOFs). Three of them specify mutual misorientation of the adjoining grains. The misorientation is represented by a rotation, which brings both grains in a perfect matching. It is defined by the rotation axis, which has two DOFs, and the angle to rotate, which has one DOF. The other two DOFs are set to describe the grain boundary plane, which is defined by the normal of the plane (two DOFs). When the misorientation between two grains is smaller than 15° , the grain boundary formed is considered to be low angle grain boundary (LAGB). LAGBs are consisting of separated dislocations. Similarly, when the misorientation between two grains is larger than 15° , the grain boundary is considered to be high angle grain boundary (HAGB).

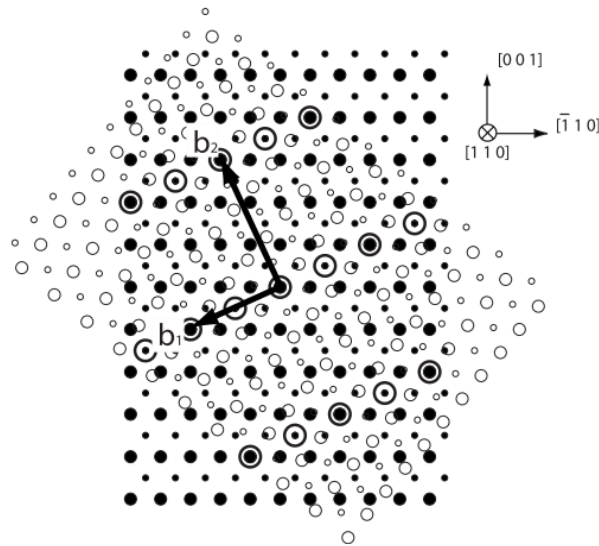


Figure 1.7 $\Sigma 11$ coincidence site lattice formed by two FCC grains, the atoms belong to one grain are colored by black while the atoms belong to the other grains are colored by white[32].

There are several models to describe grain boundaries. Coincidence site lattice (CSL) model is usually applied to study grain boundaries. When two crystal lattices share a fraction of sites at their interface, the interface is known as a coincidence site lattices boundary [33]. CSL boundaries are characterized by Σ , which is the ratio of the volume of the CSL unit cell to that of standard unit cell. Fig1.7 shows a $\Sigma 11$ CSL in FCC structure [32]. It is reported that increasing the fraction of CSL boundaries raises materials' resistance to corrosion [34], fracture [35] and creep [36][37]. In order to improve properties of polycrystalline, efforts have been made to increase the fraction of CSL boundaries through thermal and thermo-mechanical treatments [38].

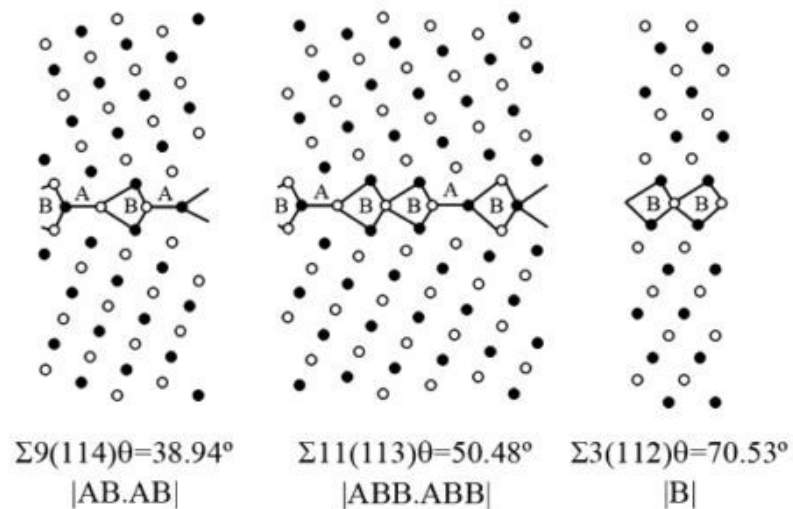


Figure 1.8 Structure units in three symmetric tilted CSL grain boundaries in BCC lattice [39].

Along with the CSL model, structure unit model was proposed to represent some CSL grain boundaries. The principle of structure unit model is to represent CSL grain boundaries by several structure units. Fig.1.8 shows that some CSL grain boundaries are divided into single or a combination of structure unit [39]. This model makes it more

convenience to describe grain boundaries' structures. However, this model is not capable to describe grain boundaries at elevated temperatures, or grain boundaries in non-equilibrium states. While in NC materials, most grain boundaries are in non-equilibrium states. These non-equilibrium GBs may significantly influence the mechanical behavior of nanostructures generated by SPD.

Due to a wide range of industrial applications of steel, GBs and CSL boundaries in α -Fe have been considerably studied, mainly on atomic configuration and mechanical properties of symmetric tilt CSL GBs (STGBs). Molecular dynamics (MD) simulation and first principle calculation are frequently employed in these studies. To characterize the atomic arrangement of $\langle 110 \rangle$ symmetric tilt boundaries, Nakashima and Takeuchi [40] proposed a MD structure unit model, which was verified by Bhattacharya *et al* [41] with DFT calculation of $\Sigma 3$ (111) and $\Sigma 11$ (332) GBs as typical $\langle 110 \rangle$ tilt GBs. Tschopp *et al* [39] studied about 170 GBs and their interactions with point defects in α -Fe, most of which are however STGBs. The interaction between brittle cracks and high-angle GBs and low-angle GBs in BCC iron at different temperatures were analyzed by Terentyev *et al* [42]. Spearot *et al* [43] proposed a tensile strength model to relate the GB structure with dislocation emission from STGBs in FCC materials. For FCC materials, some special GBs (*e.g.* STGB $\Sigma 3$ and $\Sigma 9$) with small porosities and energies show greater resistance to dislocation emission from GB areas.

However, there are still unclear issues related to the effect of GB structure on the mechanical strength. In BCC materials, dislocation emission or twinning is influenced by the GB structure, which consequently affects the overall mechanical behaviors. In addition to the loading direction relative to the GB, dislocation emission from the GB or

twinning is also influenced by the strain rate. These basic aspects have not been fully understood yet. Even for the simple case of STGBs without considering GB inclination, the correlation between the GB structure and dislocation/twinning emission from GB remains unclear.

The current CSL model is incomplete, since it only describes the misorientation between two adjacent grains without specifying the GB plane, *i.e.* the CSL model only specify the three parameters out of five parameters to define grain boundaries. Even with fixed misorientation and Σ value, the inclination of GB plane can vary, resulting in symmetric and asymmetric tilt GBs (ATGBs) with different responses to the external stress. ATGBs are more popular and observed more frequently in polycrystalline materials [33]. It is shown that GB dissociation and faceting happen to ATGBs in both simulations [32] and experiments [44], which influence the local stress fluctuation in GB region when subject to external stress. Thus, more research is needed to understand structure, energy, and mechanical properties of ATGBs in comparison with STGBs. Furthermore, the investigation of individual grain boundaries in α -iron could provide us better understandings of the deformation mechanisms of NC α -iron.

1.5 Objectives of this study

The main objective of this study is to clarify the effects of annealing treatment on the mechanical properties of NC α -iron with the help of molecular dynamics simulations.

The objectives of this research are further divided into the following aspects:

1) Mechanical properties of materials are directly related to deformation mechanisms.

Due to the crucial roles that grain boundaries play in NC metallic materials, we first

investigate the influence of misorientation and inclination on the mechanical properties of grain boundaries inside α -iron by generating and deforming a series of ATGBs and STGBs. This study could provide us basic understandings of the deformation mechanism and the main factor that determines the strength of a system.

2) In order to simulate NC metals generated by severe plastic deformations as well as subsequent annealing treatment, practical computational modeling is to be developed in this study. This study also aims to provide atomic level characterizations of material structure's evolution during annealing treatment by analysis MD simulation results.

3) Uniaxial tensile deformation is to be conducted in MD to investigate the mechanical properties of annealed and un-annealed NC α -iron. Further quantitative analysis of the deformation behaviors could explain the intrinsic effects of moderate annealing treatment on strength and ductility of NC α -iron. By clarifying the intrinsic effects of annealing treatment and behind mechanisms, we could provide new strategy and criteria to alter mechanical properties of NC metals.

2. Simulation details

With great effort made in the last several decades, molecular dynamics (MD) simulation has evolved to be a powerful tool to investigate the structures and properties of various materials. Given the interaction between atoms, MD could provide in-depth insights into the structural and mechanical behaviors of NC metals; especially those phenomena which are hardly characterized using experimental methods. For instance, MD could provide direct access to GB structures, energy states, local stress distributions and deformation behavior in NC materials.

2.1 Atomic interaction

Any atomistic simulations depend on the evaluations of atomics interactions. The most accurate description may be provided by the first-principle method based on quantum-mechanical treatment of electrons. This accurate description, on the other hand, limits the systems' sizes in first-principle simulations. MD simulation is energy-driven with taking account of the Newtonian forces acting on each atom. In MD, the atomic interaction is represented by semi-empirical potentials. Instead of involving any quantum-mechanical calculations, the semi-empirical potentials represent the system's potential energy (U) as a relatively simple function of atom positions, and the forces are then computed as derivatives of U with respect to positions.

The potential energy of a system containing N atoms, could be divided into terms depending on the coordinates of individual atoms, pairs, triplets, *etc.*[45]:

$$U = \sum_i v_1(r_i) + \sum_i \sum_{j>i} v_2(r_i, r_j) + \sum_i \sum_{j>i} \sum_{k>j>i} v_3(r_i, r_j, r_k) + \dots, \quad (2.1)$$

where the first term represents the effect of an external field (*e.g.* container walls) on the system. The second term is the pair potential, which depends on the relative position of atom i and j . The third term is the potential energy of three-body interaction. If we further simplify equation (2.1) by ignoring three-body and higher interactions, equation (2.1) becomes:

$$U \approx \sum_i v_1(r_i) + \sum_i \sum_{j>i} v_2^{eff}(r_i, r_j) \quad (2.2)$$

The pair potential of second term in equation (2.2) is regarded as effective pair potential, which includes the interactions of three-body and higher. The pairwise interaction is usually expressed in Lennard-Jones (L-J) form.[46] For instance, a typical L-J form 12-6 potential looks like:

$$v^{LJ}(r) = 4\varepsilon((\sigma/r)^{12} - (\sigma/r)^6) \quad (2.3)$$

Where r is the distance between two interacting atoms and the parameters, ε and σ , need to be chosen carefully to reasonably describe atomic interactions in materials. The pairwise potential can be used to calculate the total energy directly and is convenient to implement. However, the pairwise potential alone may not accurately represent the elastic properties of realistic solid and may give misleading results.

Daw and Baskes proposed a more accurate atomic interaction model, termed as embedded atom method (EAM) [47]. In EAM, all atoms are viewed as being embedded in the host lattice consisting of all other atoms in the system. The energy of a system is

includes two kinds of interaction, the electron density embedding energy and core-core repulsion. The total energy is given as:

$$U = \sum_i F_i(\rho_{h,i}) + \frac{1}{2} \sum_{\substack{i,j \\ i \neq j}} \phi_{ij}(R_{ij}) \quad (2.4)$$

The first term is the summation of embedding energy of atoms. The embedding energy of atom i , F_i , is a function of the density of the host at atom i 's position without atom i . ϕ_{ij} is the short-range pair potential and R_{ij} is the distance between atom i and j . The host density $\rho_{h,i}$ is simplified as the sum of atomic density (ρ_a) of the constituents, *i.e.*

$$\rho_{h,i} = \sum_{j(\neq i)} \rho_j^a(R_{ij}) \quad (2.5)$$

In this research, EAM potential of α -iron developed by Mendeleev *et al* [48] was mostly employed. The generalized stacking fault energy, interstitial and vacancy formation energy, thermal expansion and dislocation properties predicted by this potential are in good agreement with DFT data [49], which makes it effective in simulating tensile deformation of polycrystalline α -iron [50][51].

With the calculated potential energy of the system, we can then solve the classical equations of motion for a system consisting of N atoms via the potential. With Cartesian coordinates r_i , we have:

$$m_i \ddot{r}_i = f_i, \quad f_i = -\nabla_{r_i} U \quad (2.6)$$

Where m_i is the mass of atom i . Given the atomic positions, velocities, and other dynamic information along with equation (2.6) at time t , one can predict the position, velocity and

other information for each atom at time $t+\delta t$. The time step, δt , is usually chosen within the scale of several femtoseconds to cover the atoms' oscillations at their lattice sites.

2.2 Model construction

Construction of models is an important step in MD simulations. There are some different model types, *e.g.* bicrystal model [30], columnar polycrystalline model [52], full 3D model [53], *etc.* Bicrystal model is one of the most popular models to investigate interfaces in metallic materials. Fig.2.1 demonstrates a typical configuration of bicrystal model. The advantage of bicrystal model is the model's configuration could be easily controlled in this study. We employed bicrystal model to study GBs and deformation behaviors of NC iron. In the model, two grains with different orientations are placed together. Due to the three-dimensional (3D) periodic boundary conditions (PBC), there are two grain boundaries inside the system, as demonstrated in Fig.2.1.

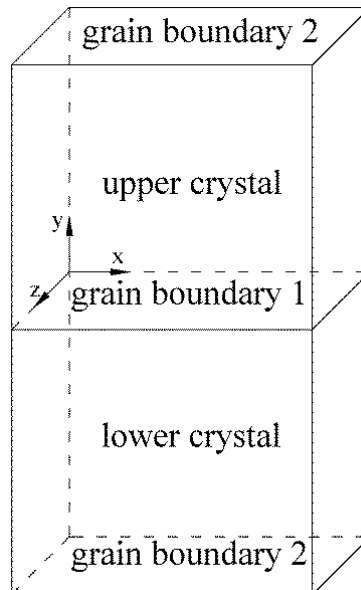


Figure 2.1 A bicrystal model employed in this study. Due to the 3D periodic boundary condition, there are two same grain boundaries in the system.

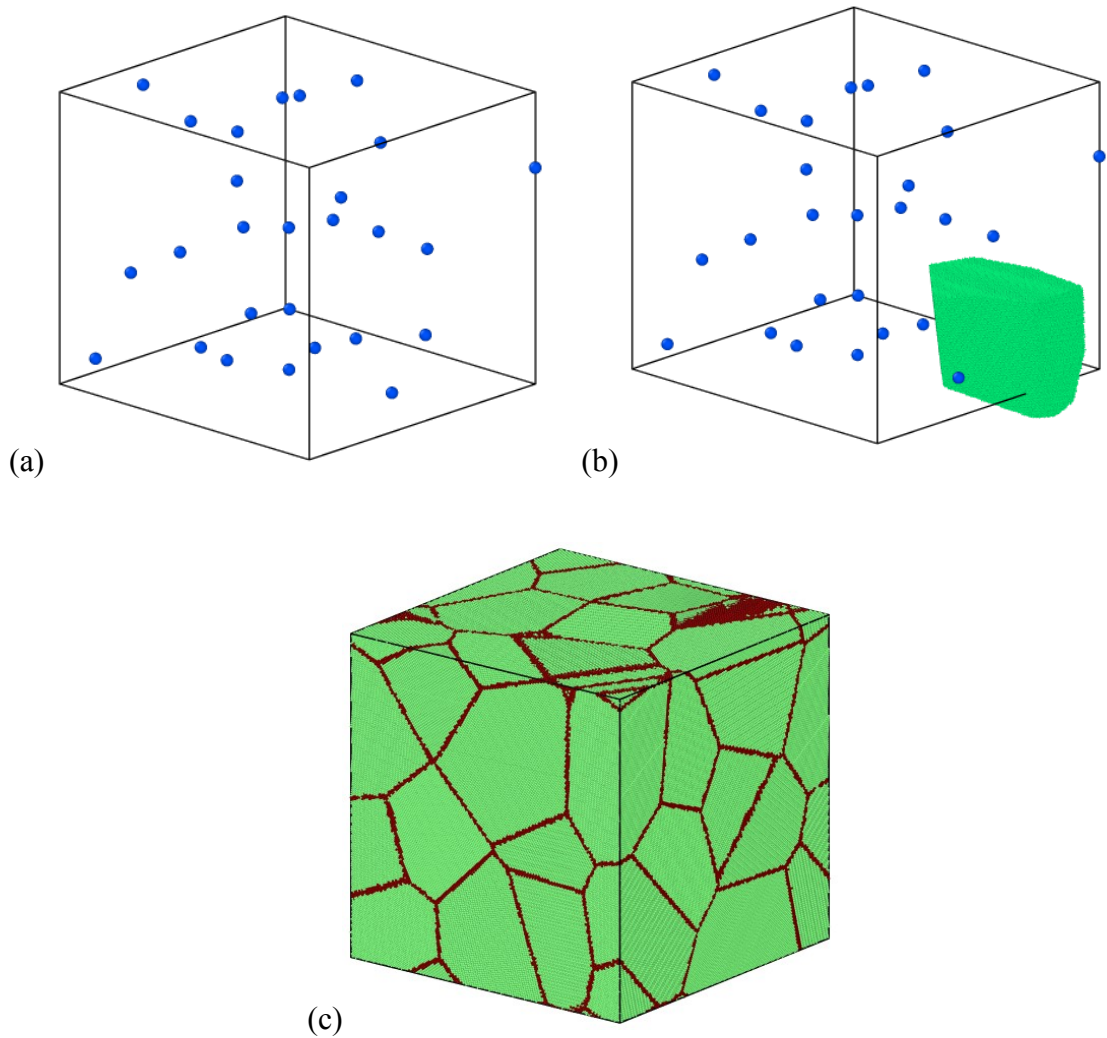


Figure 2.2 Voronoi construction is applied to build 3D polycrystalline models in this study. (a) In a $40 \times 40 \times 40 \text{ nm}^3$ cubic box, 27 seeds are randomly placed. (b) A grain with random orientation is generated from a seed. (c) The whole system is generated by Voronoi construction.

On the other hand, the advance in computing technology allows MD to be run with more atoms and larger time scale. It becomes practical to build larger and more complicated MD models, which are closer to realistic situations. For instance, applying a columnar model consisting of 4 grains to investigate mechanical properties of a material, results of

the simulation are highly influenced by the initial configuration of the system. Including a sufficient number of grains is crucial to investigate the mechanical response of materials. Here we applied Voronoi construction [54] to build polycrystalline iron system, which had 27 grains with grain size around 20nm (details given in chapter 4).

In Voronoi construction, a 3D space is divided into several small volumes based on the “closeness” to points in the 3D space. The set of points, which is usually called seeds, is specified beforehand. For each seed there is a corresponding region consisting of all points closer to that seed than to any others. To implement this algorithm, we first define a box with a certain number of seeds (Fig.2.2 (a)). For each seeds, we “grow” a bcc grain with a random orientation. The grain correspond to each seed is cut by “closeness” criteria (Fig.2.2 (b)). Fig.2.2 (c) demonstrates the whole system generated by Voronoi construction. The polycrystalline model constructed by this method is closer to real situation, compared to bicrystal models, and could take full advantage of computational resources.

2.3 Local structure identification

From MD simulation, we could obtain atomic configuration of a system at different times. One crucial issue is how to identify the local structure, *i.e.* how to determine whether an atom belongs to perfect crystals or grain boundaries or stacking faults or dislocations lines. Common neighbor analysis (CNA) [55] provides a simple and reliable approach to identify atoms’ structures. CNA method considers a pair of nearest neighbor atoms, for instance, atom α and atom β . There are three indices (j, k, l) of this pair of nearest neighbor atoms: j , which is the number of shared nearest-neighbors of this pair atoms; k is the number of bonds between shared neighbors and l is the number to

differentiate diagrams with same $j k$ indices but different bonding among common neighbors. Different combinations of the three numbers, $ijkl$, could represent different lattice structures. All nearest atom pairs in perfect FCC lattice have the index of 421. In HCP lattice, half of the nearest atom pairs have the index of 421 and the other half have the index of 422. In BCC lattice, 3/7 nearest neighbor pairs form 441 while the rest 4/7 forming 661, as shown in Fig.2.3 [55]. By CNA method, we can easily identify the atoms belonging to perfect lattice and the atoms belonging to defects, *e.g.* grain boundaries, stacking faults, dislocations, voids, *etc.*

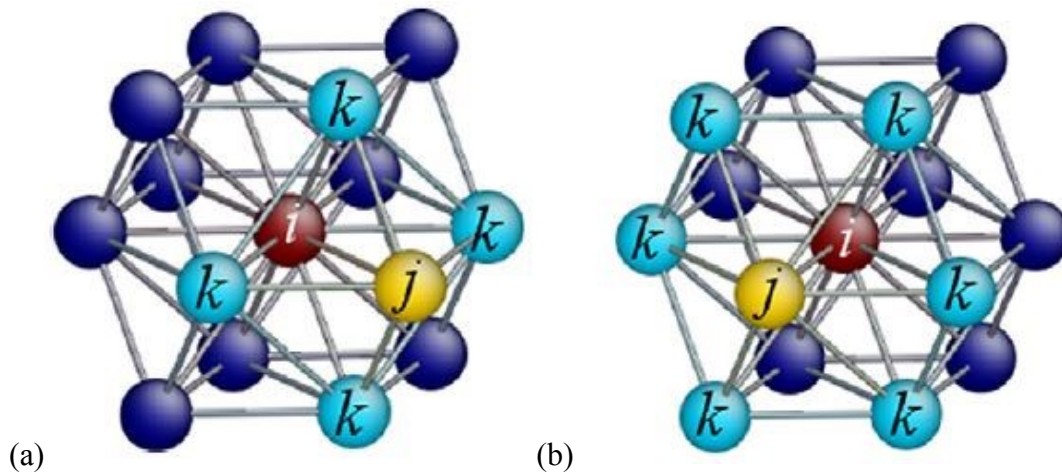


Figure 2.3 The CNA indices of (a) 441 and (b) 661 in perfect BCC lattice [55].

In a large scale MD simulation, which may be consisting of abundant interface and defects, the automatic identifications of planar defects (GBs, stacking faults) and line defects (dislocations) are required. Dislocation Extraction Algorithm (DXA) developed by Stukowski [56] is a powerful tool to extract dislocations, stacking faults and grain boundaries from MD snapshots. There are three principle steps of DXA: 1) the CNA method is used to identify crystalline atoms (*i.e.* atoms in regular lattice sites) and

disordered atoms (*i.e.* atoms in disordered lattice sites); 2) Interface meshes are constructed to separate crystalline atoms from the disordered ones; 3) In dislocation segments, initial Burgers circuit traces through the segments to get information of dislocations. DXA could automatically identify the dislocations and stacking faults inside a system, and provides the information of defects into .vtk files, which could be further visualized by Paraview. Fig.2.4 (a) shows an original system configuration colored by CNA value, while Fig.2.4 (b) shows the information of defects extracted by DXA and visualized by ParaView. The information of defects extracted from MD snapshots is beneficial to the deformation analysis in polycrystalline α -iron.

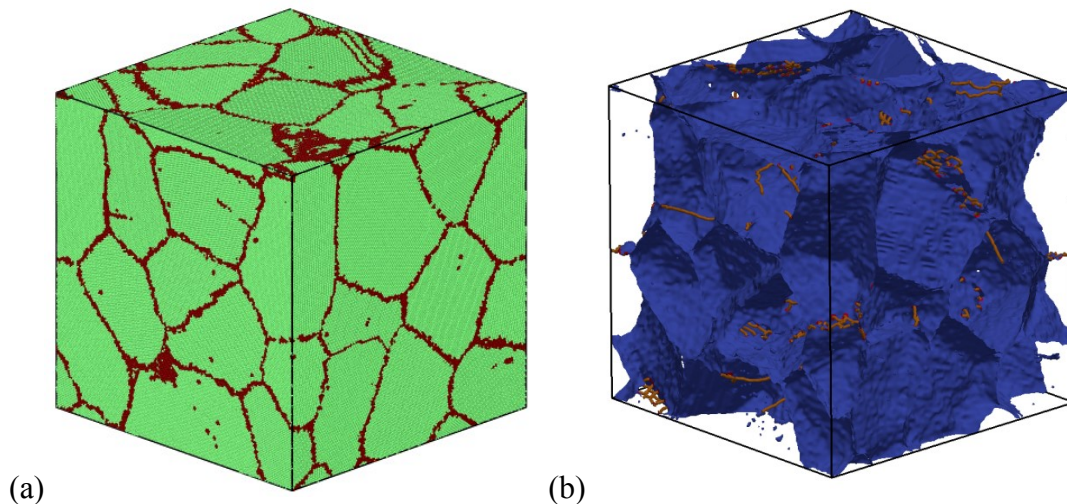


Figure 2.4 (a) Atomic configuration snapshot of a NC α -iron deformed to 8% strain, atoms are colored by CNA values. (b) Grain boundaries and dislocations information identified by DXA algorithm and plotted by ParaView. Dislocation lines are represented by red lines.

2.4 Summary

Molecular dynamics is a powerful tool for investigating the deformation behavior and mechanical properties of NC materials. In MD, the length scale could reach up to hundreds of nanometers and the time scale could reach up to several nanoseconds. By employing this technique, we could study the atomic behaviors of NC α -iron. In this study, we built full 3D polycrystalline samples, which can reflect mechanical response when subjected to external strains. With the help of CNA and DXA analysis, dislocation formation and motion in deformation processes could be clearly revealed.

To ensure the accuracy of the information extracted from MD simulations, the following aspects need to be carefully considered. The first issue is the efficiency of the interatomic potential, as all the simulation results are determined by the potential. The EAM potential developed by Mendeleev *et al* is proven suitable to simulate the deformation process of α -iron. The second issue is the limited time scale in MD simulation. As the simulation time is limited to a few nanoseconds, a typical deformation strain rate in MD simulation is around $10^{-1}/\text{ns}$ ($10^8/\text{s}$), which is several orders of magnitude greater than in experimental studies. Thus the deformation mechanisms need to be carefully verified, especially for strain rate dependent processes.

3. Deformation of NC α -iron¹

In NC metallic materials, there are a large percentage of atoms belong to or affected by grain boundaries. Grain boundaries play crucial roles in determining the mechanical properties of NC materials. To investigate mechanical properties and deformation behaviors of NC materials, we first employed bicrystal models to exam the structure and mechanical properties of individual grain boundaries in α -iron. Objectives of this study are to investigate 1) energies and structures of both coincident site lattice STGBs and ATGBs in α -Fe, 2) the strength of STGBs and its dependence on the Schmid factor and the boundary structure, and 3) deformation mechanism of ATGBs and main factors that determine the strength of ATGBs in α -Fe. To achieve the objectives, we employed the MD simulation to study a series of $\langle 110 \rangle$ STGBs and ATGBs bicrystal systems in α -Fe with misorientation ranging from 20.05° to 90.00° . Selection of the $\langle 110 \rangle$ tilt GBs for the present study is based on the fact that this type of GBs is frequently observed in polycrystalline iron and alloys [41].

3.1 Simulation configuration

The bicrystal model used in this study is shown in Fig.3.1 (a), which consists of two $\langle 110 \rangle$ oriented grains. For STGBs (Fig.3.1 (b)), both lower and upper grains are tilted with the same angle but in opposite directions in order to obtain a symmetric grain boundary. For ATGBs (Fig.3.1 (c)) in this study, the lower grain is fixed, while the upper grain is tilted to different angles, ranging from 20.05° to 90.00° . Since the periodic

¹ The results presented in this chapter have been published as:
X. Tong, H. Zhang, D.Y. Li, 2014, *Modelling Simul. Mater. Sci. and Eng.*, 22, 065016

boundary condition is applied to all x-, y- and z- directions, there are two identical GBs in each bicrystal model, as shown in Fig.3.1 (a). Ten STGBs having the same Σ values as those of corresponding ATGBs are generated, and the Σ value only depends on the misorientation between two adjacent crystals. The distance between these two identical GBs is at least 9.7nm. Detailed information on GB geometrics is provided in Table 3.1.

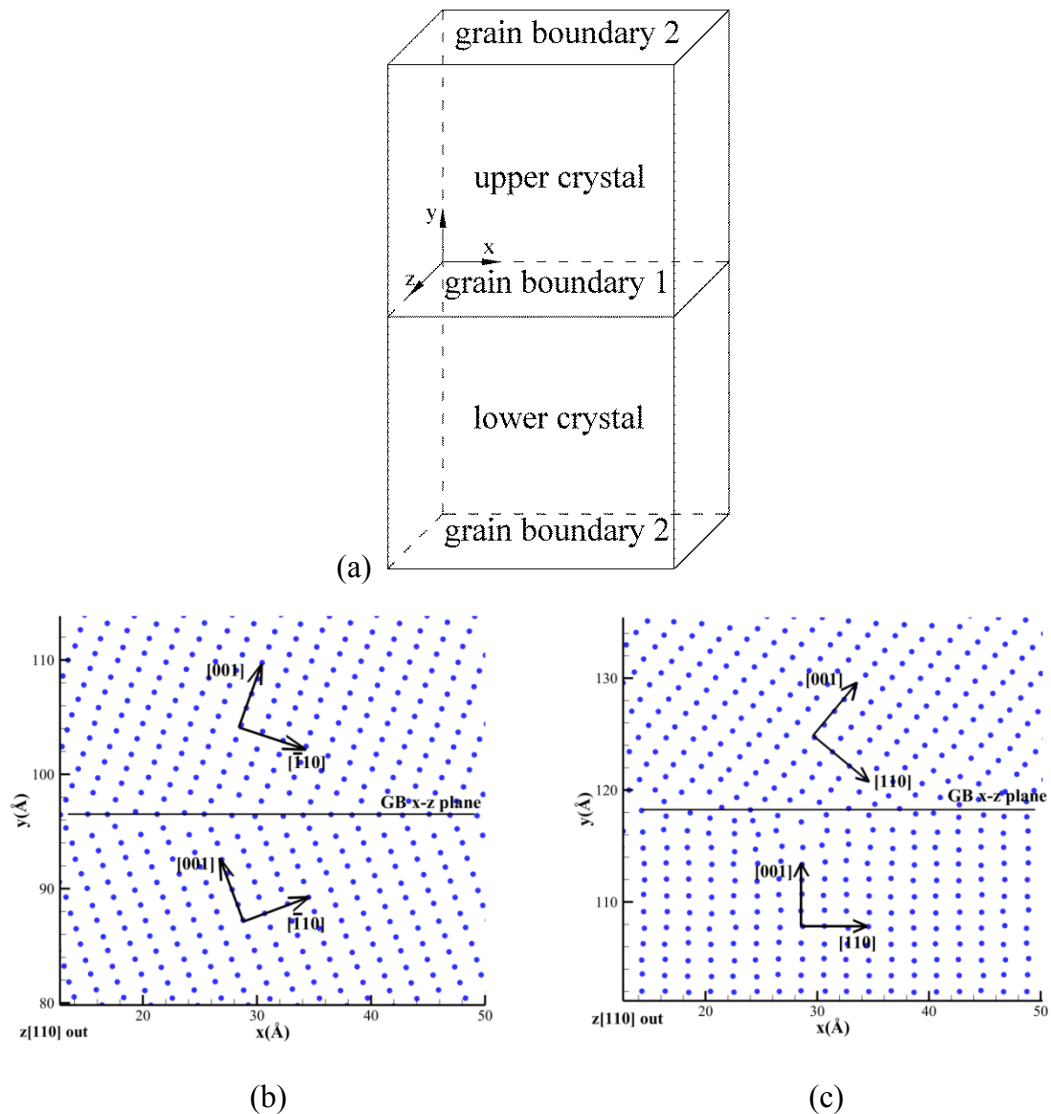


Figure 3.1 (a) The schematic of a bicrystal model. There are two identical GBs as periodic boundary conditions applied to all three dimensions. (b) Atomic configuration of

a $\Sigma 9$ STGB. Upper crystal and lower crystal are tilted with the same angle but in opposite directions to obtain a symmetric GB structure. (c) Atomic configuration of a $\Sigma 9$ ATGB. The lower grain is fixed and the upper grain is tilted with an angle of 38.94° .

Table 3.1 Grain boundary tilting angles, plane indices and system sizes of STGBs and ATGBs bicrystal systems

Σ value	$\langle 110 \rangle$ tilt angle	STGBs		ATGBs	
		Boundary plane	Size(nm×nm×nm)	Boundary plane	Size(nm×nm×nm)
$\Sigma=3$	70.53°	$(1\bar{1}2)(\bar{1}12)$	$9.9 \times 22.7 \times 3.2$	$(2\bar{2}1)(001)$	$9.7 \times 22.9 \times 3.2$
$\Sigma=9$	38.94°	$(1\bar{1}4)(\bar{1}14)$	$10.3 \times 19.3 \times 3.2$	$(4\bar{4}7)(001)$	$10.9 \times 22.9 \times 3.2$
$\Sigma=11$	50.48°	$(1\bar{1}3)(\bar{1}13)$	$10.7 \times 22.7 \times 3.2$	$(6\bar{6}7)(001)$	$8.9 \times 22.9 \times 3.2$
$\Sigma=17$	86.63°	$(2\bar{2}3)(\bar{2}23)$	$10.0 \times 22.7 \times 3.2$	$(12\bar{12}1)(001)$	$13.7 \times 22.9 \times 3.2$
$\Sigma=19$	26.53°	$(1\bar{1}6)(\bar{1}16)$	$10.0 \times 22.7 \times 3.2$	$(6\bar{6}17)(001)$	$15.3 \times 20.0 \times 3.2$
$\Sigma=27$	31.68°	$(1\bar{1}5)(\bar{1}15)$	$10.5 \times 22.8 \times 3.2$	$(10\bar{10}23)(001)$	$10.9 \times 20.0 \times 3.2$
$\Sigma=33$	58.99°	$(2\bar{2}5)(\bar{2}25)$	$9.3 \times 22.8 \times 3.2$	$(20\bar{20}17)(001)$	$13.3 \times 22.8 \times 3.2$
$\Sigma=33$	20.05°	$(1\bar{1}8)(\bar{1}18)$	$9.9 \times 22.7 \times 3.2$	$(8\bar{8}31)(001)$	$13.3 \times 22.8 \times 3.2$
$\Sigma=43$	80.63°	$(3\bar{3}5)(\bar{3}35)$	$10.6 \times 22.8 \times 3.2$	$(30\bar{30}7)(001)$	$17.4 \times 22.9 \times 3.2$
$\Sigma=57$	44.00°	$(2\bar{2}7)(\bar{2}27)$	$12.2 \times 22.8 \times 3.2$	$(28\bar{28}41)(001)$	$23.0 \times 28.5 \times 3.2$
N/A	90.00°	N/A	N/A	$(1\bar{1}0)(001)$	$11.7 \times 22.8 \times 3.2$

In the above CSL bicrystal model systems, the periodicity of the upper and lower grains is commensurate along x-direction. As an example, for the upper grain in the $\Sigma 9$ ATGB bicrystal system, the distance between two repeating periodic atoms in x-axis ($|x_{\text{upper}}|$) is $9\sqrt{2}a_0$, where a_0 is lattice parameter; for the lower grain, the distance between two repeating atoms in x direction ($|x_{\text{lower}}|$) is $\sqrt{2}a_0$. In order to achieve commensurate

periodicity between upper and lower grains, the repeat unit length of this GB equals to $|x_{\text{upper}}|$, which is nine times the value of $|x_{\text{lower}}|$. The GB length in x- direction should be integer times of the repeating unit length. Thus, there is no elastic strain when two tilted grains are combined together. Based on this calculation, dimensions of the GB models in x- and direction are set to be within the range from 89.0 to 230.6 Å. Dimensions in x-, y- and z- directions of each bicrystal system are listed in Table 1. The number of atoms in these bicrystal systems ranges from 61,440 to 182,240. Compared to other reported studies [30][39][49] on GB properties, the sizes of bicrystal systems under study are large enough to accurately evaluate energetic and mechanical properties. No GB sliding and grain rotation occurred in the present bicrystal systems when experienced uniaxial tensile deformation.

In order to reach equilibrium states for the STGBs and ATGBs during limited simulation time, isoenthalpic-isobaric ensemble (NPH) combined with velocity rescaling was applied to control the system pressure and temperature when all the bicrystal systems were constructed. To relax the whole system, the temperature of a system was raised to 700K and kept for 500ps by velocity rescaling, while the pressure in x-, y- and z- directions were all controlled at 0 bar. At the same time the temperature of grain boundary region (*i.e.* a 3nm slab parallel to and centered upon the mean boundary plane) was raised to and kept at 1000 K by additional velocity rescaling. The GB regions were relaxed at the elevated temperature for 500 ps and then cooled down to 700 K at a rate of 0.5 K/ps followed by energy minimization using conjugate gradient method until the force on atoms were below 10^{-10} eV/Å to eliminate the possible residual stress caused by temperature difference. The whole system was then cooled down from 700 K to 300 K

before further simulation was carried out. At 300 K, the atomic configurations of relaxed GBs are consistent with structure unit model [40]. For ATGBs, the relaxed structures show evidences of GB dissociation and faceting, which is observed in both simulation [32] and experimental [44] studies.

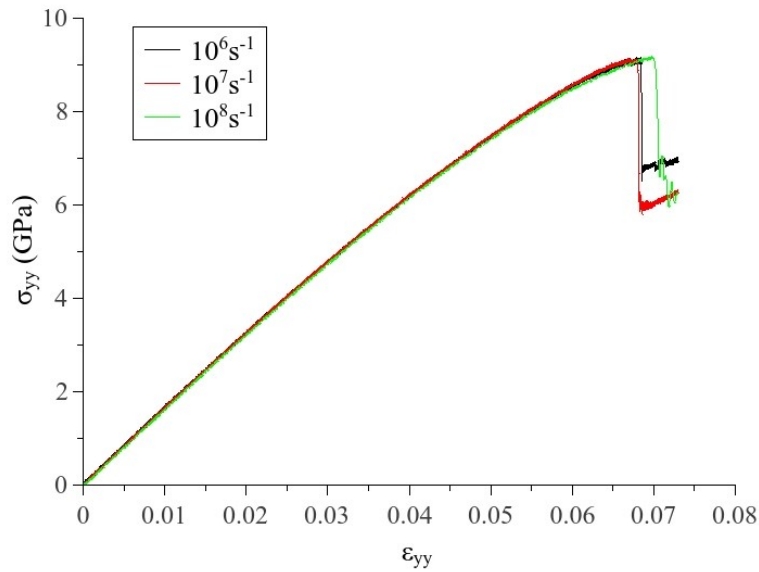


Figure 3.2 Stress-strain curves for STGB $\Sigma 9$ bicrystal system under tensile deformation with different strain rates using MD simulation. With different strain rates (10^6s^{-1} , 10^7s^{-1} and 10^8s^{-1}), the bicrystal system exhibits the same yielding behavior (twinning emission from GB areas) and the yield strength is about the same (9.16 GPa, 9.16 GPa and 9.19 GPa, respectively). The chosen strain rate, 10^8 s^{-1} , could give yield strength data with reasonable accuracy.

After relaxation of GBs, uniaxial tensile deformation in y- direction with a true strain rate of 10^8 s^{-1} was applied to all ATGBs and STGBs bicrystal system. Fig.3.2 shows stress-strain curves of $\Sigma 9$ STGB when subjected to tensile deformations at different strain rates. In Fig.3.2, the strength of $\Sigma 9$ STGB is almost the same when deformed at different strain

rates. The strain rate used in this study could give reasonable results and also save the computational time. During deformation, isothermal-isobaric (NPT) ensemble via Nose-Hoover method [57][58] was employed to control the pressures in x- and z- directions of bicrystal systems at 0 bar, and keep system temperature at 300 K.

All simulations were conducted with LAMMPS, which is developed by the Sandia National Laboratory [59]. Simulated atomic configurations are plotted by AtomEye [60]. Atomic types were identified by the common neighbor analysis (CNA) [55][61]. Atomic volumes of each Fe atom in GB areas were calculated using Voro++ code [62].

3.2 Results and discussion

3.2.1 Energy and volumetric expansion of GBs

For quantitative analysis, the GB energy of each bicrystal system was calculated using the following equation:

$$\gamma_{GB} = \frac{E_{pot.} - NE_{coh.}}{2A} \quad (3.1)$$

where $E_{pot.}$ is the total potential energy of atoms in a bicrystal system after relaxation, N is the total number of atoms in the system, $E_{coh.}$ is the cohesive energy of Fe at 300K, which is -4.0815 eV per atom, and A is the interface area between two grains. Grain boundary energies of STGBs are shown in Fig.3.3, labeled by square symbols, while the grain boundary energies of ATGB are labeled by circle symbols. For STGBs, within the range between 20.05° and 90.00°, a main cusp at 70.53° is observed, which occurs at the tilt angle of $\Sigma 3$ GB (1 $\bar{1}2$)($\bar{1}12$) (coherent twin boundary). The energy value of this cusp is 276.81 mJ/m², which agrees well with first principle simulation [63]. For ATGBs, the

trend of grain boundary energy varying with the tilting angle ranging from 20.05° to 90.00° is similar to that of STGBs. A cusp (873.79 mJ/m²) at $\Sigma 3/70.53^\circ$ is also observed, which is the grain boundary of $(2\bar{2}1)(001)$. For the same Σ value, grain boundary energies of ATGBs are always larger than those of corresponding STGBs.

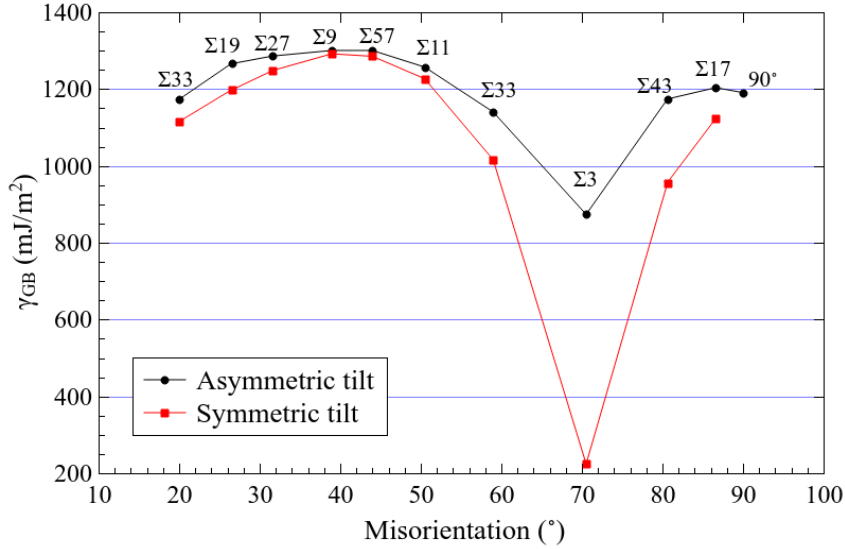


Figure 3.3 Energy of equilibrium (300 K) $\langle 110 \rangle$ symmetric (square) and asymmetric (circle) tilt boundaries with the tilt angle ranging from 20.05° to 90°. For the same misorientation angle, the GB energy of ATGB is always larger than that of corresponding STGB. The deep cusp occurs at the $\Sigma 3/70.53^\circ$ GBs.

Because of disordered atomic arrangements in the GB region, the volume of a bicrystal system is larger than that of a perfect crystal consisting of the same number of atoms. This expansion caused by grain boundaries, denoted as Δh , can be calculated by the following equation:

$$\Delta h = \frac{V_{B.C.} - NV_{S.A.}}{2A} \quad (3.2)$$

where $V_{B.C.}$ is the volume of bicrystal after relaxation, N is the number of atoms in this

bicrystal, $V_{S.A.}$ is the Voronoi volume of single iron atom in a perfect bcc crystal at 300 K, which is 11.6797 \AA^3 in the present case, and A is the interface area between two grains in the bicrystal system. The relationship between the grain boundary energy and expansion is illustrated in Fig.3.4. A larger expansion caused by GB leads to a larger deviation from a perfect crystal structure, corresponding to a higher GB energy. As shown in Fig.3.4, for both STGB (Fig.3.4 (a)) and ATGB (Fig.3.4 (b)), the GB energy is proportional to GB expansion.

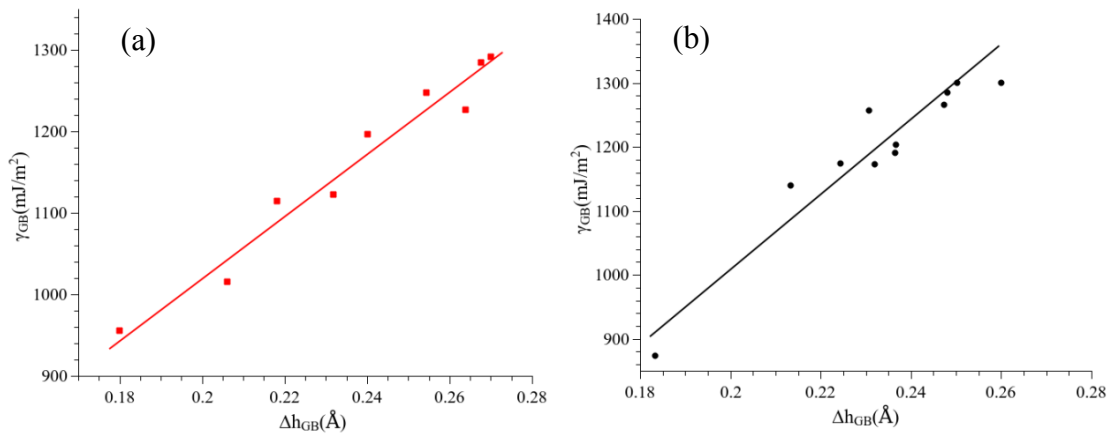


Figure 3.4 Relationship between excess volume and grain boundary energy of STGBs (a) and ATGBs (b). Symmetric $\Sigma 3$ is not included in this plot.

3.2.2 Yield pattern: twinning or dislocation emission

After relaxation, tensile deformation in y-direction is applied to all ATGBs and STGBs bicrystal systems. Results of the simulations demonstrate that twinning is mainly responsible for yielding in both the ATGB and STGB systems, while dislocations appear to play only a minor role. All ATGBs and 7 out of 10 STGBs (see details in section 3.2.3) bicrystal systems start to yield by twinning emission from GB regions with a slip system of $\langle 111 \rangle \{112\}$.

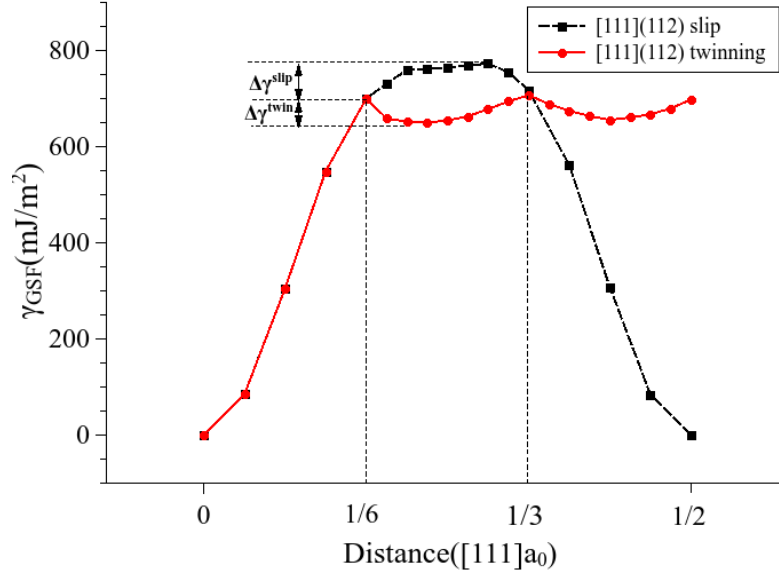


Figure 3.5 Generalized stacking fault energy of α -iron [111](112) sliding system. The energy of $a_0/6[111]$ partial dislocation sliding to form a $a_0/3[111]$ partial dislocation ($\Delta\gamma^{slip}=73$ mJ/m²) is higher than that for [111](112) twinning ($\Delta\gamma^{twin}=50$ mJ/m²), indicating that twinning is a preferred yielding mechanism.

The simulation of the tensile deformation process shows that when the shear stress resolved in tensile direction reaches a critical value, atoms start to slide in certain sliding system, which is $\langle 111 \rangle \{112\}$ in this case. To explain why twinning rather than dislocation emission from the GBs is the main yield mechanism for α -iron on the nano-scale, we examined the stacking fault energy of bcc $\langle 111 \rangle \{112\}$ sliding systems. The energy profiling on (112) plane in [111] direction is shown in Fig.3.5. During deformation, atoms slide to form an $a_0/6$ [111] partial dislocation (a_0 is the lattice parameter) first. There are two possible subsequent yield processes. If this $a_0/6[111]$ partial dislocation slides further to form a full $a_0/2[111]$ dislocation, it needs to overcome an energy barrier ($\Delta\gamma^{slip}$) of 73 mJ/m². Alternatively, if further emissions of $a_0/6[111]$

partial dislocations on successive adjacent (112) planes, the system would yield by twinning, which requires to overcome a lower energy barrier ($\Delta\gamma^{twin}$) of 50 mJ/m². Thus, twinning emission is preferred when the bicrystal system is yielded.

In both experimental and simulation studies, deformation twinning is a commonly observed in α -iron based materials, especially at low temperatures and high strain rates. Sorbello *et al* [64] observed {112} deformation twin in single crystal and polycrystalline Fe-3wt.%Si. {112} twinning was also demonstrated by Farkas's [65] atomistic studies of deformation in the crack tip region during low temperature fracture of bcc Fe single crystals. Smida and Bosansky [66] reported deformation twinning in pure polycrystalline iron in the ductile-to-brittle transition temperature region. Li *et al* [50] analyzed the stacking fault energy and showed that the $\langle 111 \rangle$ {112} twinning was preferred during the deformation of α -iron nano-wire. Based on our calculated stacking fault energies and above-mentioned studies, twinning and dislocation emission are two competitive yield mechanisms in α -iron and the former appears to be more favorable due to its lower energy barrier than that of dislocation emission on $\langle 111 \rangle$ {112} slip systems.

3.2.3 Yield strength of STGBs

The stress-strain curves of tensile deformations applied to STGBs were obtained from the simulation and are shown in Fig.3.6 (a). As mentioned in section 3.2.2, seven out of ten symmetric tilt bicrystal systems start to yield by $\langle 111 \rangle$ {112} twinning initiating in grain boundary regions. The rest three STGB bicrystal systems are $\Sigma 17$, $\Sigma 43$ and $\Sigma 33$ (58.99°). The Schmid factor of $\langle 111 \rangle$ {112} slip systems in $\Sigma 17$ and $\Sigma 43$ bicrystal systems are very small (0.1943 and 0.2414 respectively), so that $\langle 111 \rangle$ {112} slip systems could not be

activated. Consequently, these two bicrystal systems may yield not by twinning but by emitting other possible dislocations, *e.g.* $\langle 111 \rangle \{110\}$ dislocations. In the $\Sigma 33$ bicrystal system, intrinsic stacking faults occur along the GB, making it yield by dislocation emission from GBs. These three STGB are thus not discussed in the yield strength model of STGBs bicrystal systems.

For simplicity, we have thus analyzed the tensile strengths of seven $\langle 110 \rangle$ STGB bicrystal systems which yield by $\langle 111 \rangle \{112\}$ twinning emission. The yield strength of the bicrystal system varies with the tilt angle, as shown in Fig.3.6 (b). The stresses in *y*-direction are also resolved to $\langle 111 \rangle \{112\}$ twinning systems, by multiplying the yield strength by the Schmid factor, labeled by red squares in Fig.3.6 (b). As illustrated, the resolved stress does not change much as the tilt angle varies.

Spearot *et al* [43] proposed an interface strength model to analyze the strength of $\langle 110 \rangle$ STGB bicrystal systems in FCC materials, in which the Schmid factor and GB porosity are taken into account. Since GB energy is more general and thermodynamically related to the behavior of GBs, we modify this strength model and express it as:

$$\sigma_{yield} = (1 - \xi \gamma_{GB}) \frac{\tau_{ideal}}{\mu SF} \quad (3.3)$$

where ξ is an influence parameter of GB energy on the yield strength, γ_{GB} is the GB energy, τ_{ideal} is the ideal shear stress of $\langle 111 \rangle \{112\}$ slip system (7.2 GPa [34]) calculated based on the density functional theory, μ is the influence factor of Schmid factor, and SF represents Schmid factor of slip systems, which decomposes the uniaxial applied stress into the resolved shear stress acting on the slip plane along the slip direction.

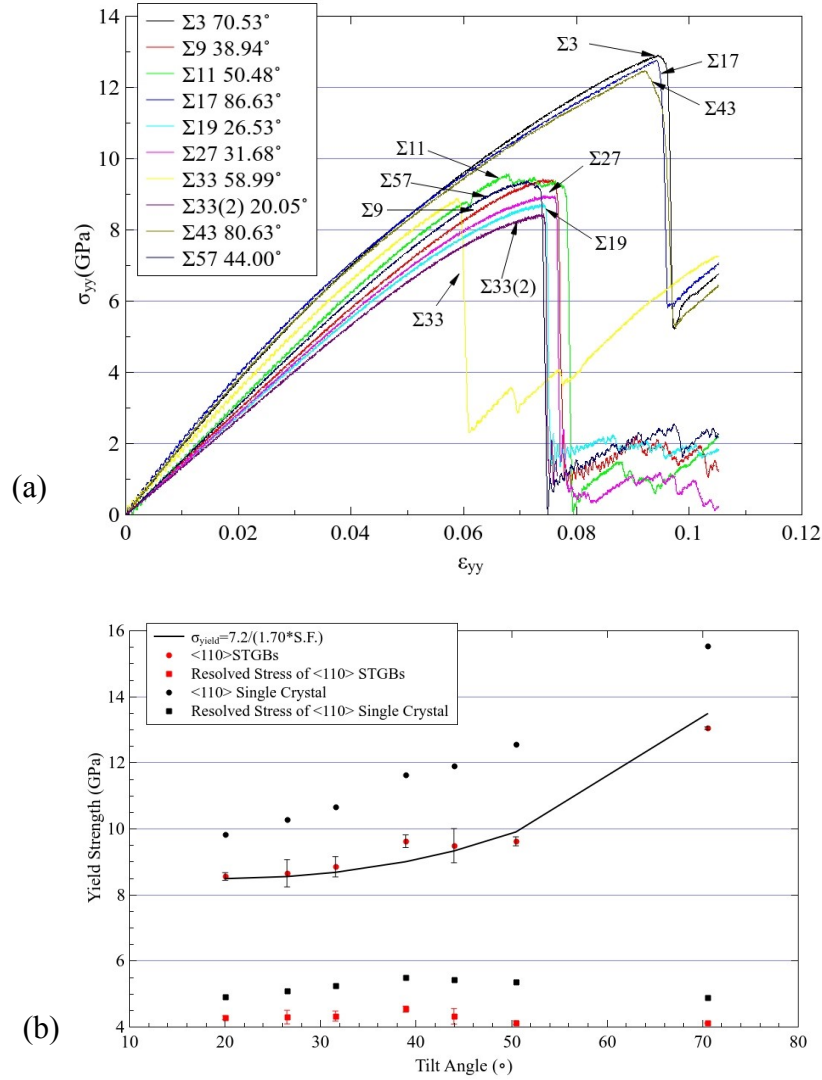


Figure 3.6 (a) Stress-strain curves of STGBs bicrystal systems. The tensile strain rate is 10^8 s^{-1} . (b) Yield strengths of $\langle 110 \rangle$ STGBs bicrystal systems with the tilt angle in the range of $20.05^\circ \sim 70.53^\circ$, and that of corresponding single crystal. Yield strengths are also resolved to $\langle 111 \rangle \{112\}$ slip systems, as labeled by square symbols.

Values of ξ and μ were determined with the least squares regression technique. ξ is assumed to be positive, as larger grain boundary energy could possibly decrease the yield strength of bicrystal systems. The best fitted value of ξ and μ are 0 and 1.70, respectively.

Thus, the yield strength model of STGB bicrystal systems becomes:

$$\sigma_{yield} = \frac{7.20}{1.70SF} (GPa) \quad (3.4)$$

Equation (3.4) implies that the yield strength of STGBs system is mainly governed by Schmid factor, while theoretically the GB energy does not influence the yield strength. The predicted values of yield strength are presented in Fig.3.6 (b) by solid line, which match well with the simulation results.

In order to verify the strength model, uniaxial tensile deformations are also applied to single crystals, results of the simulation are compared to those of STGBs. As illustrated in Fig.3.6 (b), the overall yield strength and resolved stress of single crystals are larger than that of bicrystal systems. From Fig.3.6 (b), it is suggested that introducing STGBs of different misorientations into single crystals may result in roughly the same amount of decrease in yield strength. Bearing in mind GB energy varied with misorientation as shown in Fig.3.3, this support that the GB's yield strength is insensitive to GB energy in α -iron.

For further confirmation, we increased the energy of GB in $\Sigma 3$ STGB bicrystal system from 276 mJ/m² to 467 mJ/m² by introducing vacancies into the GB. As expected, the added vacancies do not affect the overall yield strength of the system (only leads to a very slight decrease in yield strength from 13.09 GPa to 13.08 GPa). These observations are consistent with Equation (3.4). The insensitiveness of the yield strength to the STGB's energy is possibly attributed to the relatively stable and perfect structure of symmetric tilt CSL GBs.

3.2.4 Yield strength of ATGBs: local stress analysis

The yielding behavior of ATGBs is different from that of STGBs. Since ATGBs are more popular in polycrystalline materials but less understood, it is of importance to investigate ATGBs in order to maximize the benefits from engineering grain boundaries.

As shown in Fig.3.1 (c), for ATGBs bicrystal systems, the lower grain is fixed, and the upper grain is tilted to different angles. For most of the ATGB bicrystal systems (except $\Sigma 17$ and $\Sigma 43$), Schmid factors of the slip planes in the lower grain are always larger than or equal to those of the slip planes in the upper grain. This means that when tensile deformation is applied to these systems, the stress resolved to $\langle 111 \rangle \{112\}$ slip systems in the lower grain is always larger than that resolved to the same slip system in the upper grain (tilted grain). As a result of the larger resolved shear stress, the ATGBs bicrystal systems start to yield by emitting twinning into the lower grain. The Schmid factors of $\langle 111 \rangle \{112\}$ slip systems in the lower grain of all ATGBs are the same. If yield strengths of the ATGBs systems are affected by the Schmid factor in a way similar to that for the STGBs, ATGBs' strengths should be of similar values.

However, as shown in Fig.3.7 (a), the yield strengths of these systems vary between 8.09 GPa and 9.30 GPa. This is different from the observed behavior of STGB systems in section 3.2.3, where the Schmid factor dominates the yield strength of the bicrystal systems. In addition, by plotting the yield strength versus the GB energy, one may see that the yield strength is roughly proportional to the GB energy as illustrated in Fig.3.7 (b). Such a trend is opposite to traditional thought that GB with a lower energy should have a larger resistance to slip [67].

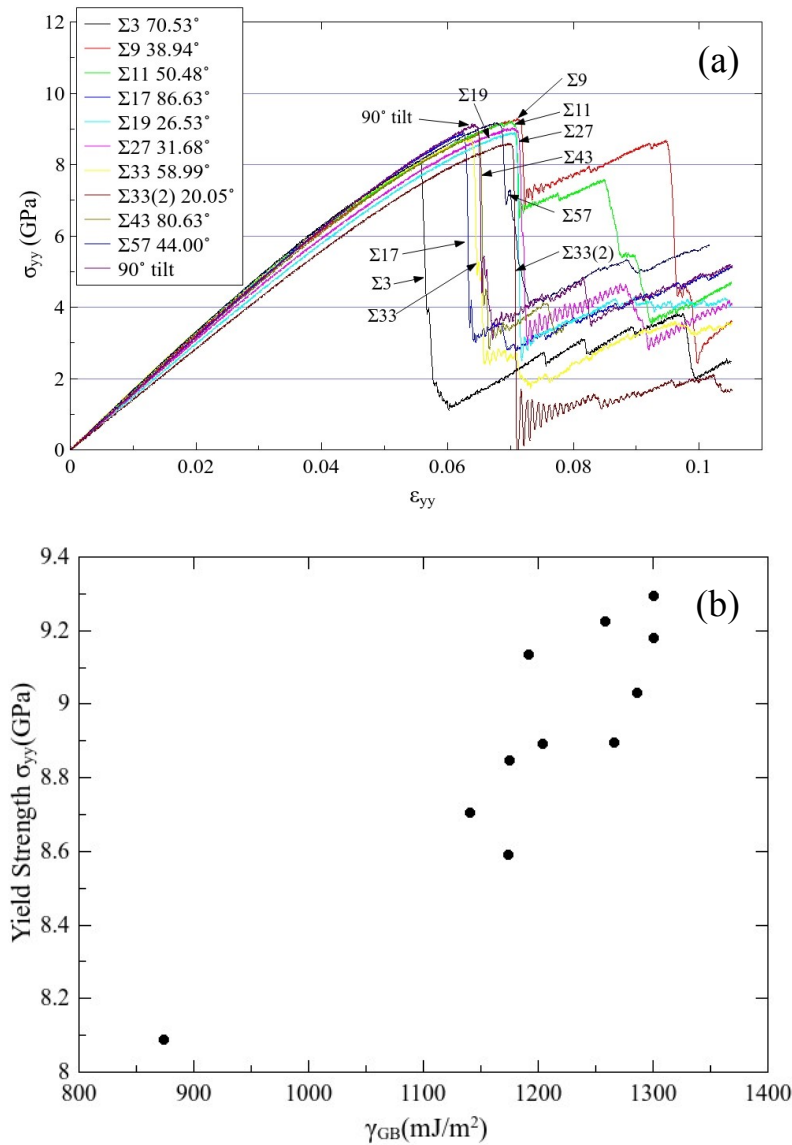


Figure 3.7 (a) Stress-strain curves of ATGB bicrystal systems. (b) The relation between the GB energy and yield strength. Yield strength is roughly proportional to the GB energy.

To understand this phenomenon and difference in yielding behavior between STGBs and ATGBs, we look at local boundary configuration and related events. Since ATGBs have higher degree of disordering, yielding process could be more heterogeneous, governed by

local stress rather than the overall stress. It is expected that the local stress could trigger yielding event when it reaches a critical value.

To verify this expectation, local stress distributions in GB regions were calculated. The stress of each atom in y- direction was calculated by LAMMPS:

$$S_{yy} = -\frac{1}{V_{S.A.}} [mv_y v_y + \frac{1}{2} \sum_{n=1}^{Np} (r_{1y} F_{1y} + r_{2y} F_{2y})] \quad (3.5)$$

where $V_{S.A.}$ is the Voronoi volume of each atom. The first term in the parentheses is a kinetic energy contribution to the stress. The second term is a pair-wise energy contribution where n loops over the Np neighbors of the atom, r_{1y} and r_{2y} are the positions of two atoms in the pairwise interaction, and F_1 and F_2 are the forces on the two atoms resulting from the pairwise interaction. As atoms' fluctuations around the lattice site may result in very high local stress, a time average procedure was applied to calculate the stress per each atom before yielding. When the system was deformed to the stage where it was about to yield, an NVT ensemble was applied to hold the system. The stress tensors of each atom in y- direction were recorded every 1 picosecond for 20 times (20 picoseconds), and converted to time-averaged values.

With the above procedure, normal stress in y- direction of each atom was calculated. Fig.3.8 shows the stress distribution in a $\Sigma 9$ ATGB bicrystal system before yielding (*i.e.* the overall stress in y- direction is close to 9.30 GPa). As shown, the stress distribution at the GB area is heterogeneous and local stresses at some points along the GB are very high, while the stress distribution inside the crystal is homogenous.

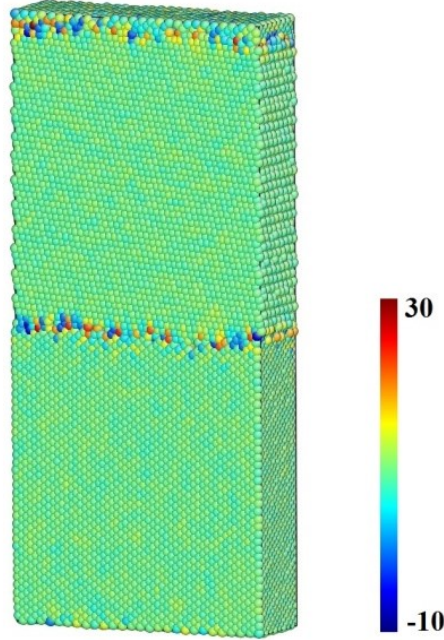


Figure 3.8 Stress distribution along a $\Sigma 9$ ATGB in a bicrystal system before yielding. The stress inside the crystals is homogenous, while that at the grain boundary is heterogeneous. The legend is in the unit of GPa.

In order to better understand the stress fluctuation at the grain boundary, the stress in the GB region is calculated as a function of the distance in x- direction. At a point x in GB area, in the range between x and $x+\Delta x$, the stress is defined as:

$$S_{ave.} = \frac{1}{N} \sum_{i=1}^N S_{yy}^i \quad (3.6)$$

where N is the number of atoms whose x- coordinate is between x and $x+\Delta x$, S_{yy}^i is the stress in y- direction of atom i . In the calculation, Δx is set as 1 Å. Fig.3.9 (b) illustrates the local stress distribution along the $\Sigma 9$ grain boundary before yielding.

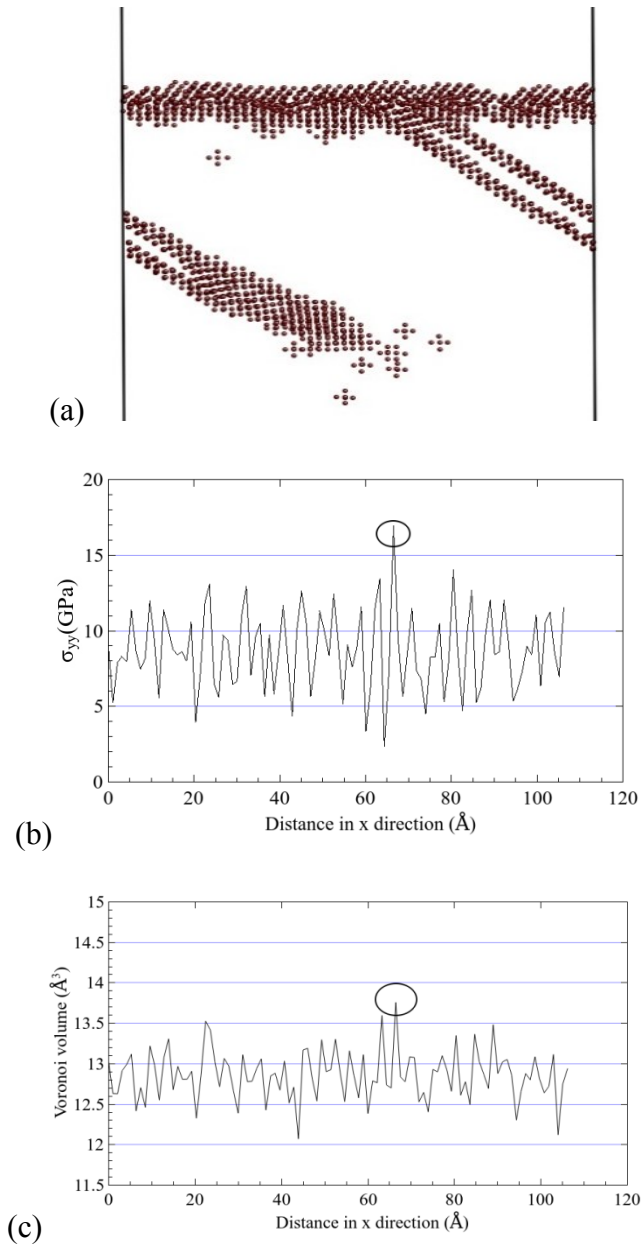


Figure 3.9 (a) In $\Sigma 9$ ATGB bicrystal system, twinning is emitting from grain boundary area into crystal. Only atoms in the GB or twin boundary are plotted. (b) Local stress distribution as a function of the distance in x- direction of the $\Sigma 9$ ATGB. The local stress varies from 2 GPa to 17 GPa. The local stress at the location where twinning emitted is the highest and so is the Voronoi volume as shown in (c). This verifies that the twinning emission from the GB area is triggered by stress-assisted free volume fluctuation.

The local stress at the $\Sigma 9$ grain boundary varies from 2 GPa to 17 GPa. Fig.3.9 (a) and (b) demonstrate that the location where twinning is emitted from the grain boundary has the highest local stress of 17 GPa. The Voronoi volume of each atom at grain boundary area before yielding is calculated as a function of the distance in x- direction by the similar method expressed by equation (3.6). As the twinning nucleation is triggered by stress-assisted free volume migration [68], the local free volume at the location of twinning emission is also the highest, as shown in Fig.3.9 (c).

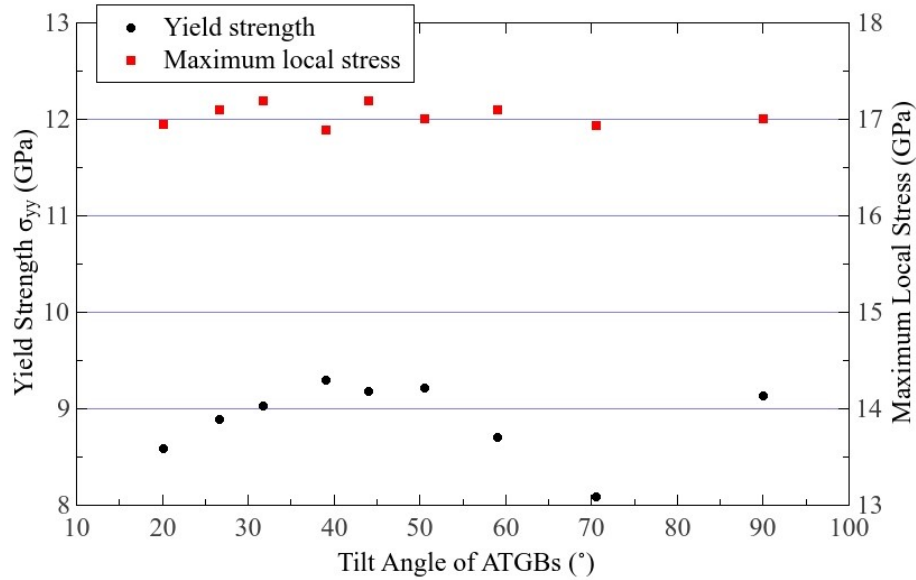


Figure 3.10 Overall yield strengths and maximum local stresses versus the tilting angle for different ATGB systems (except $\Sigma 17$ and $\Sigma 43$).

The yield strengths and highest local stresses versus tilting angle for different ATGBs are plotted in Fig.3.10. In these bicrystal systems, $\langle 111 \rangle \{112\}$ twinning emitted into the lower grain, but the overall yield strength varies from 8.09 to 9.30 GPa. However, the maximum local stresses of these ATGBs systems are at the same level (17.05 ± 0.15 GPa). This suggests that there is a critical local stress value to trigger yielding events in GB

areas, thus determine the overall strength of ATGBs.

3.2.5 Comparing the stress distribution of ATGBs and STGBs

As mentioned earlier, the CSL model only describes the misorientation between two crystals without specifying the inclination of GB. The inclination of GB could significantly influence the stress distribution and fluctuation along GB, which results in different behaviors of ATGBs and STGBs. Fig.3.11 (a) and (b) illustrate atomic arrangements at symmetric and asymmetric tilt $\Sigma 3$ GBs, respectively. The structure of $\Sigma 3$ STGB is a perfect twin boundary. However, the $\Sigma 3$ ATGB is rough and some segments were tilted to coherent twin boundary (*i.e.* symmetric $\Sigma 3$ in a more stable state) during relaxation. This local structural variation at grain boundary is responsible for the local stress fluctuation. As shown in Fig.3.11 (c) and Fig.3.11 (d), the stress fluctuation in symmetric $\Sigma 3$ GB is significantly lower than that in the asymmetric $\Sigma 3$ GB. This well explains the unusual yielding behavior of ATGBs.

Based on the local stress distribution and discussions presented in previous sections, it is clear that the yield behavior of a bicrystal system is influenced by both the Schmid factor and the atomic arrangement in GB area, which affect the local stress distribution along GB. Lower average GB energy does not necessarily result in a higher energy barrier to defect emission, which is more governed by the local stress. As shown by the bicrystal system containing ATGB, local stress fluctuation rather than the average GB energy dominates local defect emission, which triggers yielding of the entire system.

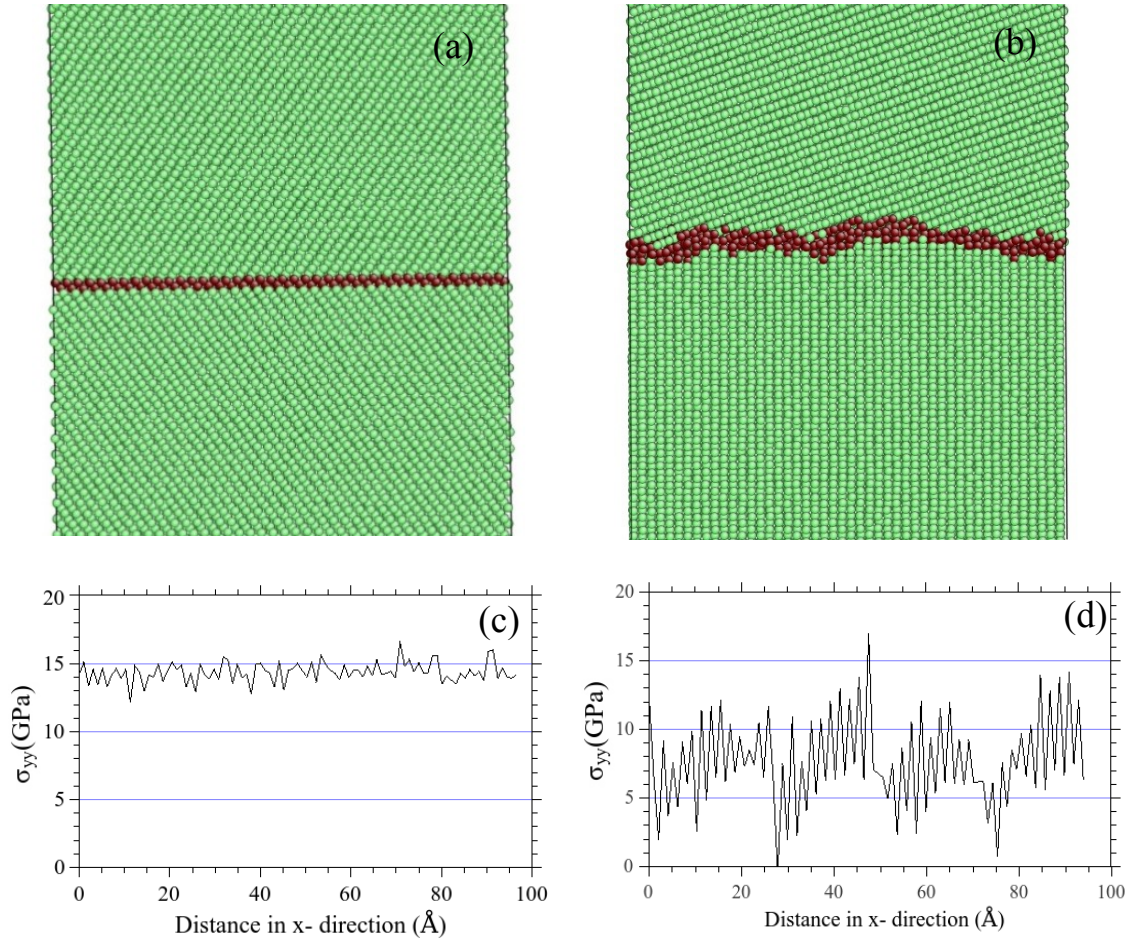


Figure 3.11 Atomic arrangements of (a) symmetric tilt $\Sigma 3$ grain boundary and (b) asymmetric tilt $\Sigma 3$ grain boundary, after relaxation at 1000 K. (c) Stress distribution of $\Sigma 3$ STGB along GB before yielding. (d) Stress distribution along $\Sigma 3$ ATGB before yielding. Green atoms belong to bcc crystals and red atoms belong to GB areas.

In the grain boundary engineering, great efforts have been made to increase the fraction of low-energy Σ GBs, especially $\Sigma 3$ GBs [38]. However, the present study indicates that special attention should be paid to the local stress distribution and inclination of the CSL boundaries relative to the external loading direction. These factors must be taken into account when fabricating textured materials for a larger fraction of CSL boundaries, since the ATGBs are more popular and their behavior is dominated by local processes due to

higher degree of disordering at the boundaries.

3.3 Summary

In summary, molecular dynamic simulation is employed to study the structure, deformation behavior, and interfacial strength of both $\langle 110 \rangle$ ATGBs and STGBs in α -iron using the EAM potential. Bicrystal systems containing ATGBs and STGBs having misorientation ranging from 20.05° to 90° were studied. It is demonstrated that with the same misorientation, GB energies of ATGBs are always higher than those of STGBs. The GB energy is proportional to the GB volumetric expansion, and such a relationship is applicable to both ATGBs and STGBs. When tensile deformation is applied to STGBs and ATGBs bicrystal systems, in the $\langle 111 \rangle \{112\}$ slip systems, twinning appears more competitive than dislocation emission from grain boundary at yielding. The former has a lower energy barrier than the latter according to generalized stacking fault energy analysis. However, this does not exclude emissions of dislocations in other slip systems, *i.e.* $\langle 111 \rangle \{110\}$ and $\langle 111 \rangle \{123\}$. During the deformation of NC α -iron, dislocation emission and deformation twinning are both possible deformation mechanisms.

The study demonstrates that the apparent strengths of CSL symmetric tilt GBs are mainly governed by Schmid factor. At the stage of yielding during tensile deformation, the stresses resolved to $\langle 111 \rangle \{112\}$ slip systems in different STGBs bi-crystal systems are almost the same. The strength of CSL GBs in α -iron is rather insensitive to GB energy. Excluding the effects of Schmid factor, the cohesive $\Sigma 3$ GB does not demonstrate higher strength even it has lowest excess energy. This is different from the situation in FCC structures, where cohesive $\Sigma 3$ GB has larger interface compared with other CSL GBs.

The ATGBs show different yielding behaviors, compared to STGBs. The yield strength of ATGBs bicrystal systems is mainly determined by the local stress at GB rather than the overall stress and average GB energy. During tensile deformation, when the local stress in ATGB areas reaches a threshold value, twinning emits from GB areas with the highest local stress. The threshold local stress value in deformation direction could serve as the quantitative intrinsic yielding criterion for $\langle 111 \rangle \{112\}$ slip systems in α -iron.

The conclusion that the overall strength of a system is determined by the local stress concentration could also be applied to $\langle 111 \rangle \{110\}$ and $\langle 111 \rangle \{123\}$ slip systems in α -iron. In NC α -iron generated by SPD process, the non-equilibrium GBs structures are anticipated, as well as other defects. While annealing treatment could reduce the local stress concentrations, annealing treatment could possibly strengthen NC α -iron according to the conclusion in this chapter. Further investigations will be presented in next chapter.

4. Effects of annealing treatment²

To clarify mechanisms responsible for the effects of annealing on NC metals, we conducted a molecular dynamics (MD) simulation study. The main objectives of this study are to investigate effects of annealing on strength and ductility of deformed NC materials and demonstrate that annealing/recovery treatment is an essential step to turn a SPD microstructure into a well-defined nanocrystalline one with superior mechanical properties.

4.1 Simulation details

A polycrystalline α -iron with grain size ranging from 18 nm to 23 nm was generated from Voronoi construction[54], shown in Fig. 4.1 (a). In a cubic box having a size of 40×40×40 nm³ and 3D periodic boundary conditions, 27 “seeds” were randomly distributed. Grains with random misorientations were generated from the “seeds” and filled the box with about 5.5 million atoms. For convenient dislocation analysis, the misorientations between adjacent grains were controlled to be larger than 15° in order to avoid low-angle grain boundaries (LAGBs). EAM potential was used to represent the interatomic force of α -iron, developed by Mendelev *et al* [48]. All MD simulations were carried out with LAMMPS [59].

² The results presented in this chapter have been published as:
X. Tong, H. Zhang, D.Y. Li, 2015, *Scientific Reports*, 5, 8459

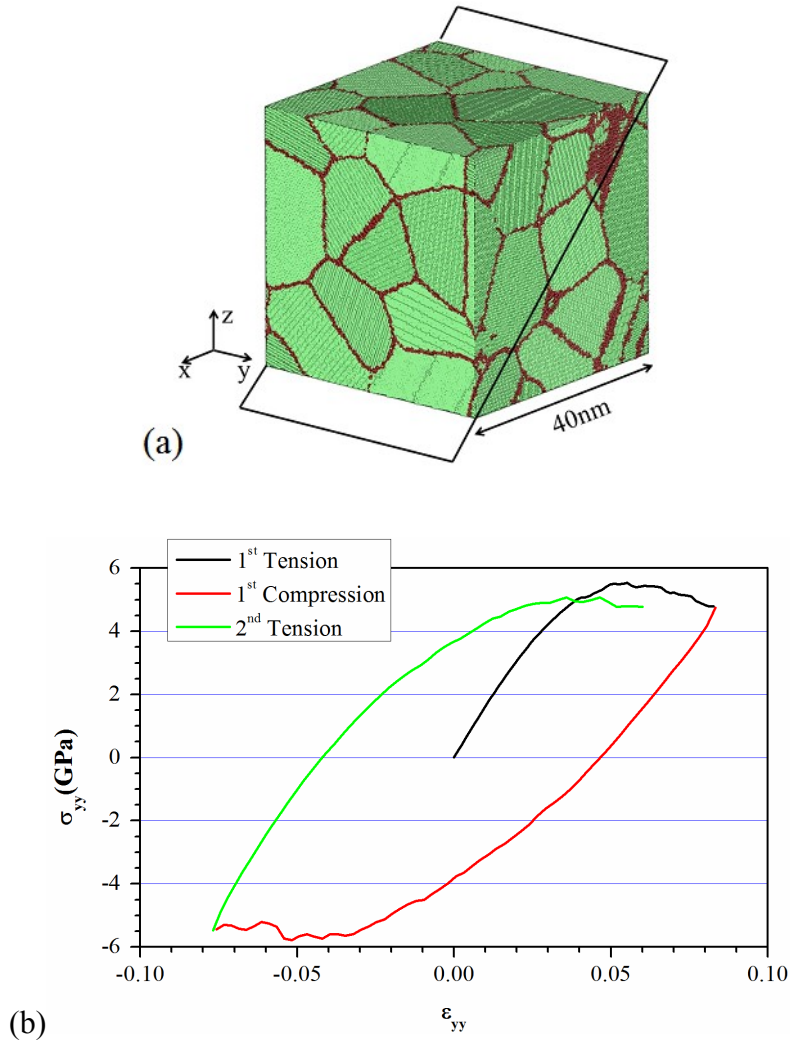


Figure 4.1 Snapshot of the system configuration (a) and stress-strain curves of cyclic load(b) applied to the system in order to simulate NC α -iron.

MD simulations were conducted using isothermal-isobaric (NPT) ensemble via Nose-Hoover thermostat [57][58]. The initially constructed system was relaxed at 700 K for 500 picoseconds (the time interval is 1 femtosecond) to reach more stable GB structures. The model system was then cooled to 300 K at a cooling rate of 2 K/picoseconds; during the cooling progress, pressures in x-, y- and z- directions were controlled at 0 bar. In order to mimic a SPD progress, cyclic loading in y-direction was applied to the

polycrystalline system. Tensile and compress deformations were introduced during cyclic loading at a strain rates of 10^{-1} ns^{-1} . The system was first pulled to reach a strain of 8% and then compressed to a strain of -8%, followed by a final tensile process up to 6% strain to avoid porosity inside the system. Corresponding stress-strain curves are shown in Fig.4.1(b). Compared to the other artificially generated GBs[24][23], the atomic structure in present simulated NC system experienced plastic deformation could be closer to the configuration of NC α -iron generated by SPD.

After above-mentioned cyclic loading, sample systems were kept at 300K and 0 bar for 200 picoseconds. Two sample systems were created, one was in as-processed state and the other was annealed. For the annealed system, it was relaxed at 750 K for 1.6 ns followed by cooling to 300 K. The time interval was 2 femtoseconds. The heat treatment curve is shown in Fig.4.2. Due to the limitation of simulation time, the annealing temperature in MD simulation was set to be higher than those in experimental studies, so that more atomic ordering could be achieved within the simulation time without grain coarsening. Such computational annealing treatment reflects experimental low-temperature annealing (typically around $0.2\sim 0.3 T_m$) or recovery treatment[16][18][19][20]. In order to test the mechanical properties, uniaxial tensile deformations with a strain rate of 10^{-1}ns^{-1} at 300K were applied to both the systems in y-direction until failure. During uniaxial tension, the pressure in x- and z- directions was kept at 0 bar. Systems were visualized using Ovito [69] and AtomEye [60]. All simulations were carried out in the Bugaboo Dell Xeon clusters provided by WestGrid.

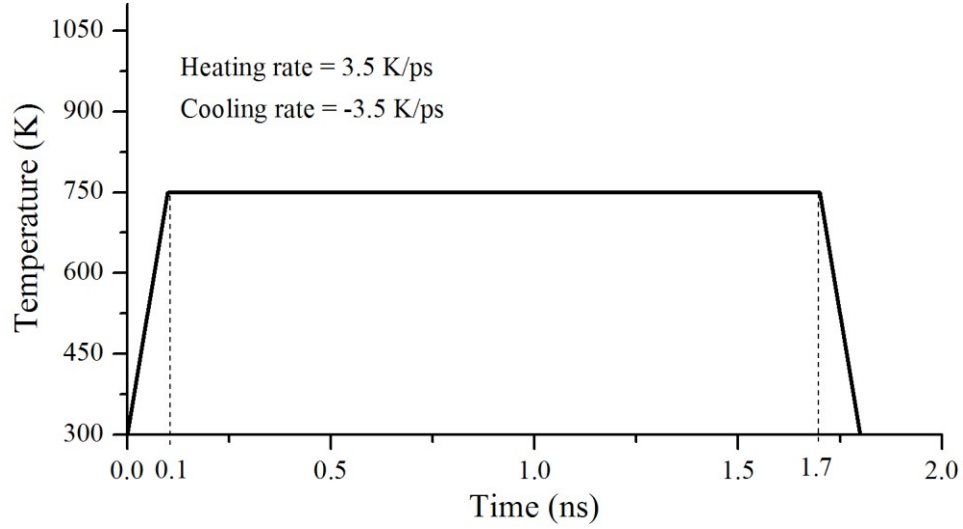


Figure 4.2 Heat treatment curve of the annealed sample. To anneal the system, the sample are heated to 750 K and kept for 1.6 nanoseconds.

4.2 Results

4.2.1 Voronoi volume and residual stress

We calculated the Voronoi volumes, hydrostatic pressures and normal stresses in y -direction (σ_{yy}) of each atom in as-processed and annealed systems. Before determining the Voronoi volume of each atom, energy minimization was carried out using a conjugate gradient algorithm until the force on every atom was smaller than 10^{-8} eV/Å. After the energy minimization, the Voronoi volume of each atom was calculated using Voro++[62]. As atoms' fluctuations around the lattice sites may result in very high local stress, a time-average procedure was performed while calculating local stress. The stresses of each atom were recorded every 4 femtoseconds within 100 femtoseconds, and then averaged to eliminate the influence of atom fluctuation. The stress component (σ_{yy}) was calculated in *virial* form. The hydrostatic pressure was represented by $-(\sigma_{xx}+\sigma_{yy}+\sigma_{zz})/3$.

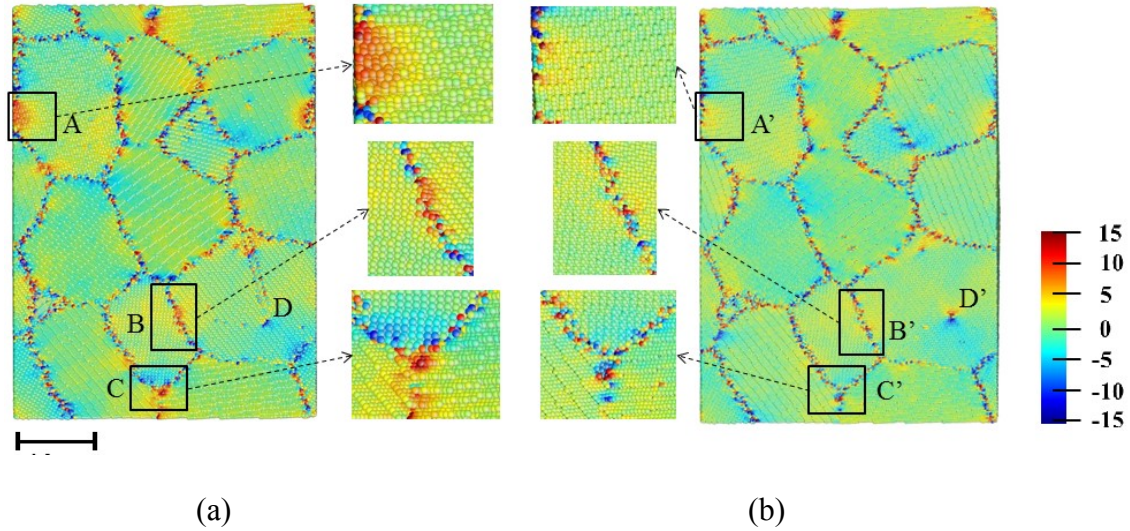


Figure 4.3 Cross-section plots of residual stress (σ_{yy}) in (a) as-processed and (b) annealed systems. The plane in Fig.4.1(a) sketched by black lines is the plane of cross-section views displayed in (a) and (b). The pressures in x-, y- and z- directions are 0 bar and the temperature is 300K. Atoms are colored by σ_{yy} ; color map is in unit of GPa. The scale bar is 10nm. Comparisons between (a) and (b) indicate that annealing treatment has reduced the internal stress, driven grain boundaries and triple junctions to more equilibrium states and converted a deformation twinning(region D in (a)) to a $\langle 111 \rangle \{112\}$ edge dislocation(region D' in (b)).

Figure 4.3 shows cross-sectional views of as-processed system (a) and annealed one (b), in which atoms are colored by their normal stresses in y- direction (σ_{yy}). Comparing Fig.4.3 (a) with Fig.4.3 (b), the stress distribution in the annealed sample is more homogenous than that in the as-processed sample. For instance, the high local stress in region A of the as-processed sample was markedly reduced by annealing, as shown in region A'. Clearly, the annealing drove the system closer to a more equilibrium state with reduced local stress and ordered atomic structures (also see those shown in regions B and

B' (GB), C and C' (triple junction) in Fig.4.3 (a) and (b), respectively). Annealing also turned a $\langle 111 \rangle \{112\}$ twinning in as-processed sample (region D) into a stable $\langle 111 \rangle \{112\}$ edge dislocation (region D'). This conversion of the planar defect to a linear defect may also decrease the system's energy[70].

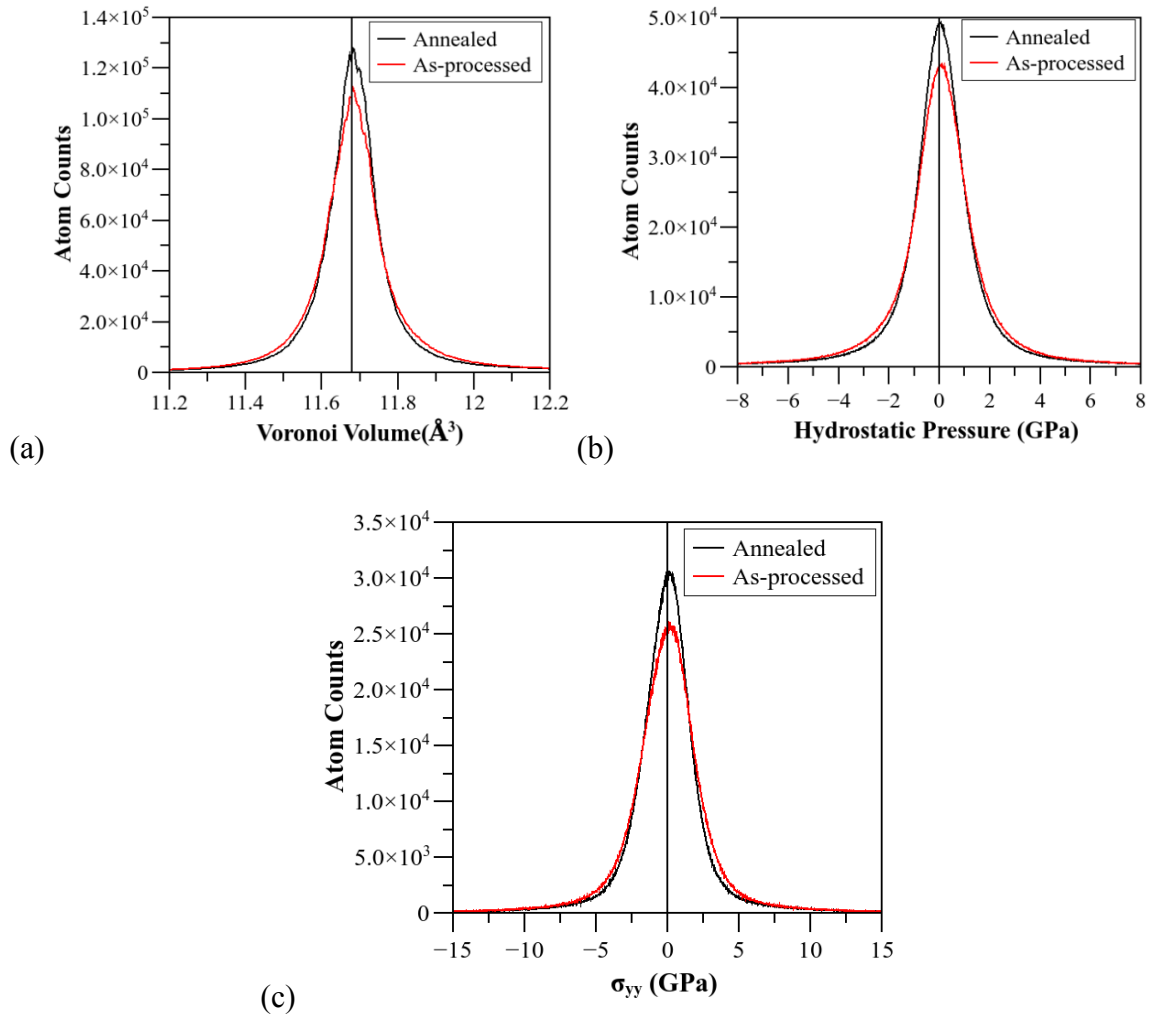


Figure 4.4 Statistical distribution of (a) Voronoi volume, (b) hydrostatic pressure and (c) normal stress in y-direction of each atom in both annealed and as-processed systems. These histograms quantitatively demonstrate more ordered atomic structures (represented by Voronoi volume) as well as reduced residual stress in the annealed system.

Figure 4.4 illustrates statistical distributions of calculated Voronoi volume, hydrostatic pressure and stress in y- direction (σ_{yy}) of each atom in both systems. At 300K, the equilibrium Voronoi volume of an iron atom in perfect BCC structure is 11.68 \AA^3 . In Fig.4.4 (a), the histogram of Voronoi volume shows that Voronoi volumes of more atoms are close to 11.68 \AA^3 in the annealed system than in the as-processed system. The distribution of hydrostatic pressure of each atom shows the same trend, *i.e.* more atoms in annealed sample are in states closer to the equilibrium one (0 GPa). The distribution of stress in y- direction (σ_{yy}) is consistent with hydrostatic pressure distribution. Note that the overall system stress is 0 GPa in all three directions; ideally most atoms should also have local stress at the level of 0 GPa. However, as illustrated in Fig.4.4 (b) and (c), residual stresses still exist, caused by the experienced cyclic loading. The local residual stress can reach up to 20 GPa. In NC metallic materials with abundant GBs, local atomic structures and local stress fluctuations at GB areas play crucial roles in determining materials' overall strengths[70][71][72]. The different atomic configurations and residual stress distributions of annealed and as-processed system should influence their overall mechanical properties.

4.2.2 Tensile deformation test

In order to evaluate mechanical properties of as-processed and annealed samples, uniaxial tensile deformation with a strain rate of 10^{-1} ns^{-1} at 300K was applied to both the systems in y-direction until failure (the time interval is 2 femtoseconds). During deformation, the pressure in x- and z- directions was kept at 0 bar by NPT ensemble. The ductility of each system, which was the plastic strain at failure, was measured.

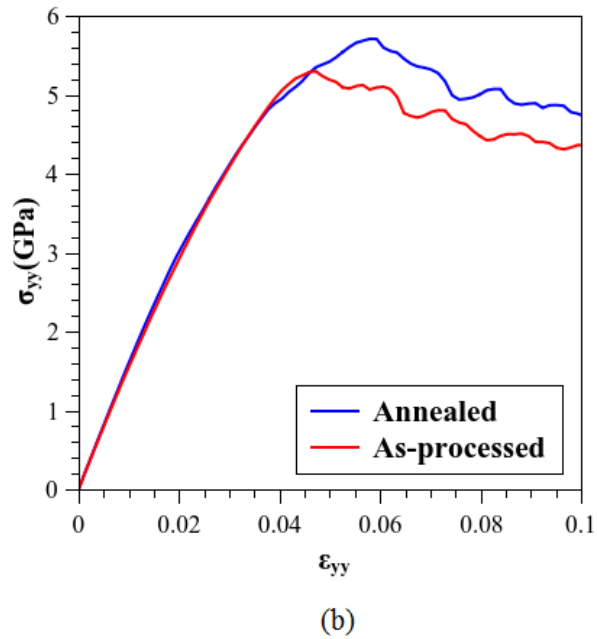
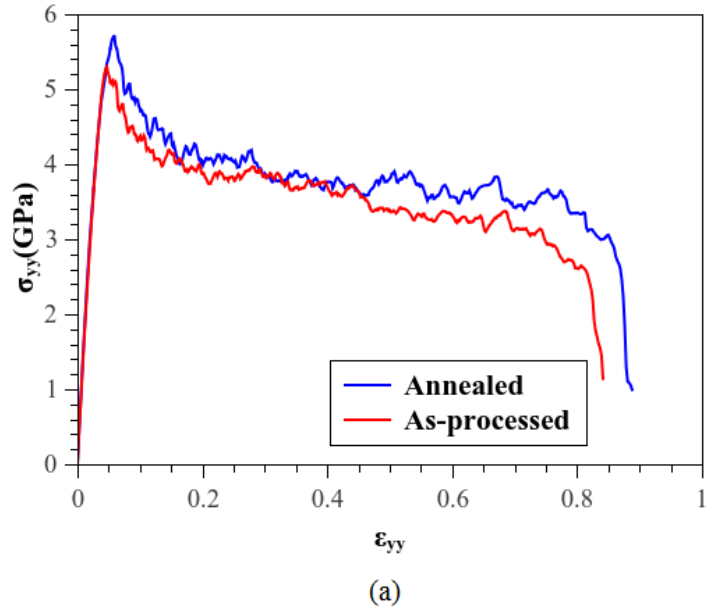


Figure 4.5 Stress-strain curves of (a) tensile deformation applied to as-processed sample and annealed sample from no strain to failure, and (b) enlarged stress-strain curves of an early deformation stage up to 10% strain.

Stress-strain curves of uniaxial tensile deformation in y- direction are illustrated in Fig.4.5. As shown, the annealing treatment increased the maximum stress and flow stress

of NC α -iron, which is consistent with experimentally observed “anneal hardening”. Besides, the ductility of NC α -iron was also improved by annealing, *i.e.* the failure strain is increased from 80% to 86%. In experimental studies, the nominal overall fracture strains of NC metals are less than the values obtained from the simulation. This could be attributed to the fact that experimentally the fracture zone often experiences very large true strain. For instance, grains in shear bands in NC Fe are deformed to true strain of 2-3 when the overall strain is 14%.[78] Corresponding values of the mechanical properties are presented in Table 4.1.

Table 4.1 Mechanical properties of annealed and as-processed systems. σ_{\max} , the maximum stress during tensile deformation; $\sigma_{\text{flow}(\varepsilon<0.2)}$, the flow stress before 20% strain; $\sigma_{\text{flow}(\varepsilon>0.2)}$, the flow stress from 20% strain to failure; $\varepsilon_{\text{failure}}$, the plastic strain at failure and K, the toughness.

	$\sigma_{\max}(\text{GPa})$	$\sigma_{\text{flow}(\varepsilon<0.2)}(\text{GPa})$	$\sigma_{\text{flow}(\varepsilon>0.2)}(\text{GPa})$	$\varepsilon_{\text{failure}}$	K(GPa)
Annealed	5.72	4.57	3.70	0.86	3.31
As-processed	5.30	4.31	3.47	0.80	2.89

4.2.3 Dislocation emission during yielding

The overall deformation behavior (mainly the plastic deformation) is directly related to dislocation activities. When the grain size is below 100nm and above 10nm (without the inverse Hall-Petch relation), dislocation emission from grain boundaries largely contributes to plastic deformation, strongly affecting the yield strength and maximum strength of a system. Dislocation emission is a highly localized behavior, and the internal stress concentrators at grain boundaries in bulk NC metallic materials could act as

dislocation emission source [72].

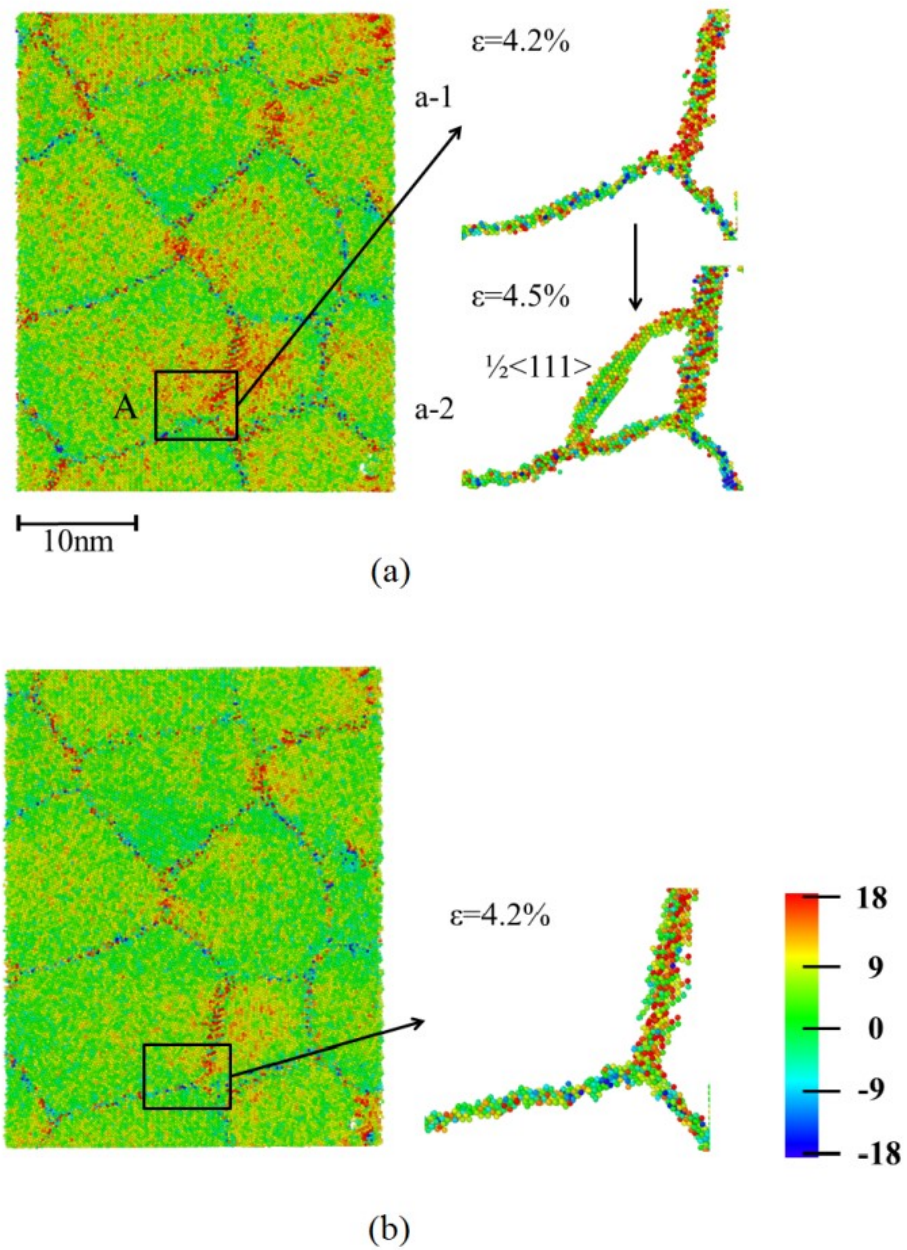


Figure 4.6 The cross-section views of (a) as-processed sample and (b) annealed sample at 4.2% strain. Atoms are colored by stress tensor in y- direction (σ_{yy}). Color map is in the unit of GPa. The high local stress of region A in as-processed sample (a) at the strain of 4.2% (a-1) results in emission of a $\frac{1}{2}\langle 111 \rangle$ dislocation at the strain of 4.5% (a-2). At

the strain of 4.2%, local stress in the same region in annealed sample (b) is more homogenous, and no dislocation is emitted from this region when deformed further.

In this study, the maximum strength of the annealed system is 8% higher than that of as-processed one, as shown in Fig.4.5 and Table 4.1. The as-processed sample reaches its maximum strength of 5.30 GPa at 4.6% strain. The local stress distribution of the as-processed sample before reaching the maximum strength was analyzed. Figure 4.6(a) shows a cross-sectional view of stress (σ_{yy}) distribution in the as-processed sample. Figure 4.6 (a)-1 is an enlarged view of a triple junction region (marked by “A”), where high local stress is present. When the system was further deformed from the strain of 4.2% to 4.5%, a $\frac{1}{2}\langle 111 \rangle$ dislocation emitted from the triple junction, as shown in Fig.4.6 (a)-2. Fig.4.6 (b) shows the cross-sectional view of stress distribution in the same location in the annealed sample when it was deformed to a strain of 4.2%. As shown, the local stress is less inhomogeneous, and no dislocation was emitted when the strain was increased to 4.5%. The local stress analysis verifies that annealing treatment reduces the amount of active sources for dislocation emission, thus strengthening the material. Larger stress is required in order to cause dislocation emission in the annealed system.

Although GBs in annealed sample are less easy to emit dislocations, as the system is further deformed with an increase in the applied stress, other dislocation sources can be activated. Dislocation emission determines the system’s maximum strength and also influences further plastic deformations and consequently the system’s ductility.

4.2.4 Ductility

The ductility is the plastic strain at fracture, which is directly related to the fracture

behavior. For BCC [73] and FCC [26][74] materials, simulation studies show that fracture of NC materials is mostly in the intergranular failure mode. In BCC structures without truly close-packed planes, nucleation and growth of intergrain crack/voids are alternative ways to relieve strain energy during tensile deformation, especially at large strains. The cross-sectional views in Fig.4.7 show the process of crack nucleation, growth, coalescence and system failure in as-processed sample during tensile deformation. The annealed system has the same failure mode of intergranular cracking with the as-processed system.

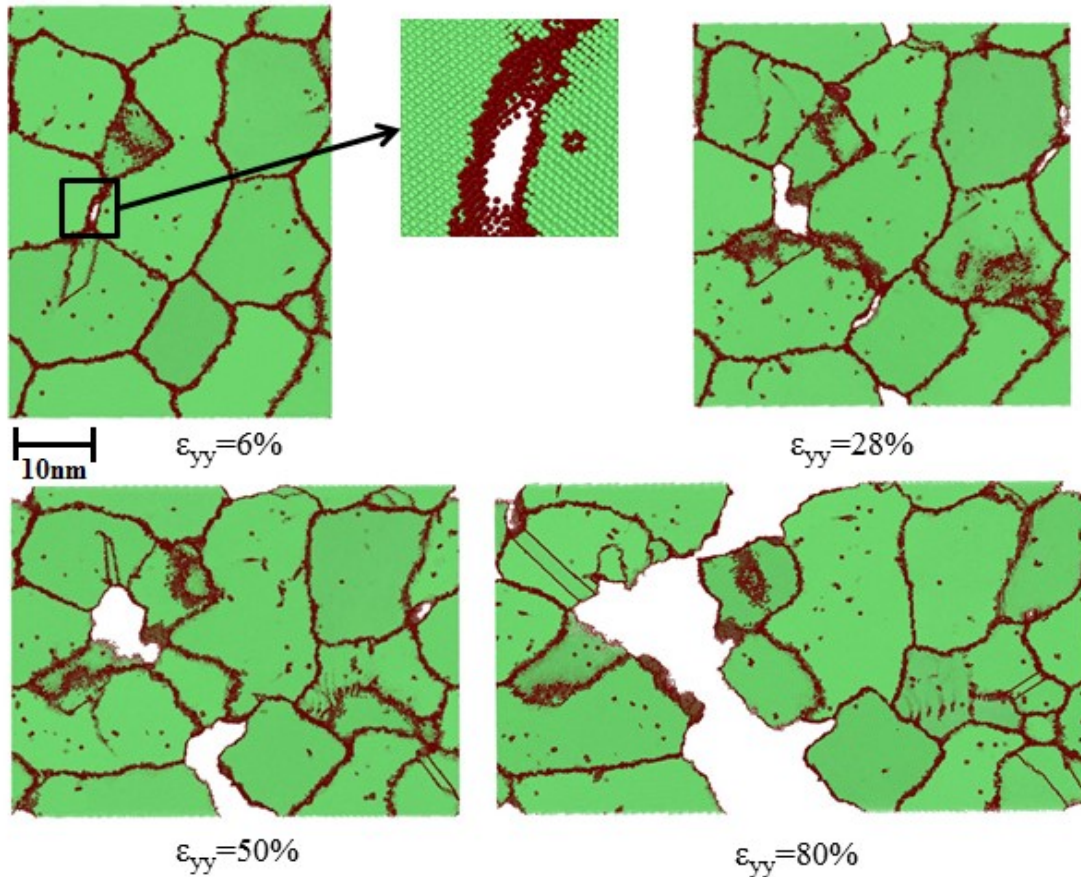


Figure 4.7 Cross-section views of atomic configurations of the as-processed system during tensile deformation. Atoms are colored by CNA values, while red spheres

represent GB and dislocation atoms, green spheres are BCC atoms. As the strain increases, the deformation process includes voids/cracks nucleation, growth and coalescence and eventual failure at 80% strain. The annealed system has the same failure mode of intergranular cracking with the as-processed system.

To quantitatively analyze the fracture process, we propose a simple method to calculate changes in the volume fraction of cracks (*i.e.* the ratio of the crack volume to the total volume of the system) during deformation. As 3D periodic boundary condition was applied to the system, identified atoms with large Voronoi volumes can be considered to be associated with nano cracks/voids inside the system. At 300K and 0 bar, the Voronoi volume of a perfect BCC atom is 11.68 \AA^3 . If one atom is associated with a nano void or crack, the Voronoi volume of the atom will be significantly larger than that of perfect BCC atom or atoms belonging to dislocations and GBs. In a perfect single crystal, if we delete several atom layers to generate a crack, of which the energetic state is close to that of free surface, then the Voronoi volume of crack atoms can be applied to identify voids and cracks in polycrystalline materials. For the Mendelev potential applied in this study, the Voronoi volume of $\{100\}$ crack surface atom is 28.8 \AA^3 , while 23.3 \AA^3 for $\{110\}$ crack surface atoms and 33.3 \AA^3 for $\{111\}$ crack surface atoms. Here we choose the average value (28.5 \AA^3) as a critical value to determine whether an atom is at crack surface. Any atom with Voronoi volume higher than critical value is identified as a void/crack atom and volumes of such atoms are summed up as the total crack volume inside the system.

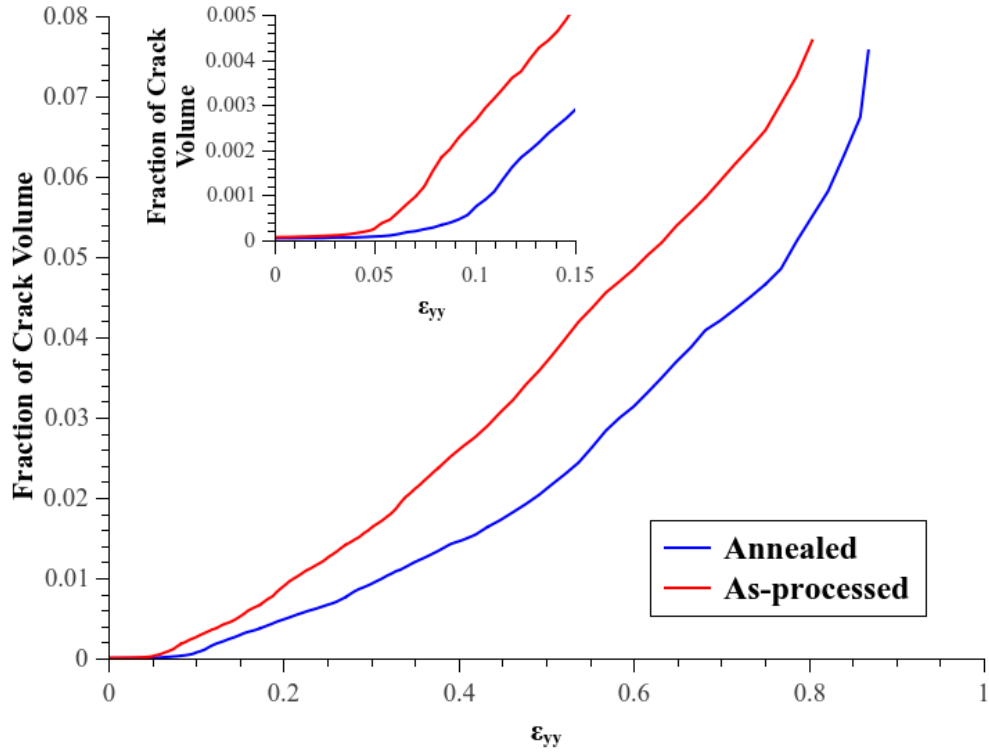


Figure 4.8 Evolution of crack fraction (crack volume/system volume) with tensile strain for annealed and as-processed samples. The inset plot shows details in the early deformation stage with the strain ranged from 0 to 15%. The annealed sample shows a larger resistance to intergranular cracking than as-processed sample.

Calculated volume fractions of cracks as a function of strain for both annealed and as-processed samples are shown in Fig. 4.8. The inset plot in Fig. 4.8 shows changes in the crack fraction in the early deformation stage before 15% strain. Compared with that in the annealed sample, crack/void nucleation occurred in the as-processed sample at smaller applied strains. The volume fraction of cracks/voids in the as-processed sample is always larger than that of the annealed sample at the same strain level. As the GBs in annealed sample have been equilibrated by annealing, they show higher resistance to intergranular cracking. The difference in crack fraction between the annealed and as-

processed samples shown in Fig.4.8 well explains why the annealed sample's ductility is 7.5% higher than that of the as-processed sample.

4.3 Discussion

In this study, annealing treatment is demonstrated to alter the structure of SPD-processed NC α -iron, *i.e.* reduce defect density and equilibrate GBs' energetic states without recrystallization and grain growth. In experimental studies, such atomistic structural evolution can be achieved by carefully tuning the annealing temperature, duration and other relevant parameters. For instance, defect minimization without grain growth in NC metallic materials during annealing treatment have been observed in NC aluminum [4], titanium [17], nickel [16], copper-nickel alloys [7] and nanocrystallized stainless steel [2]. Typical annealing temperatures employed in these studies are around 0.2~0.3 T_m (melting temperature) to avoid grain growth. In NC pure α -iron, grain size was stabilized around 18nm after annealed at 0.26 T_m [20] and no grain growth was observed at the room temperature due to lack of sufficient thermal energy. The defect ordering or minimization and GBs equilibration benefit NC materials. The present computational study has clearly demonstrated that the low-temperature annealing or recovery treatment improves the mechanical properties of SPD-processed α -iron.

Deformation of NC metallic materials involves various possible mechanisms, *e.g.* grain rotation [29], GB sliding [75], GB diffusion [30], dislocation emission [14], twinning [70][76], cavitation [26][74] at GBs *etc.* Previous studies regarding the effects of annealing treatment mainly focused on dislocation emissions from grain boundaries[4][24][23]. However, competition and synergy between different deformation

mechanisms are important to understand NC materials' mechanical properties[26]. There could be a single dominating mechanism or a mixture of multiple mechanisms, determined by lattice structure, atomic bond strength, grain size [14], strain level [26], strain rate [77] and deformation temperatures [52], *etc.* In the present α -iron polycrystalline system with grain size about 20nm, we observed a strong dependence of deformation mechanisms on the strain level. In the early deformation stage, the yield strength and maximum strength of the system are mainly determined by dislocation emission from grain boundaries. Due to the relatively low energy barrier of $\langle 111 \rangle \{112\}$ twinning compared with $\langle 111 \rangle \{112\}$ dislocation [50], deformation twinning is also observed. Given the fact that the internal stress concentrations at grain boundaries could facilitate yielding process and determine the overall strength [72], the beneficial effect of grain boundary equilibrations on NC metals' strength can be expected. We have explicitly demonstrated that the annealed system is strengthened by the reduced amount of dislocation/twinning emission sources. After a certain amount of plastic strain (6% ~ 8% engineering strain) is introduced, intergranular voids/cracks start to nucleate at grain boundaries. In BCC metals without truly close-packed planes, formation of intergranular voids/cracks provides an alternative path for relaxing the strained system. Intergranular voids/cracks grow and coalesce when the system is further deformed. In this case, the deformation involves a combination of dislocation/twinning emission from GBs and intergranular voids/cracks nucleation and growth. As the strain continuously increases, intergranular cracking becomes predominant before the NC α -iron's eventually fails. The method proposed in the work quantitatively characterizes intergranular cracking process and demonstrates that annealed NC α -iron has better resistance to intergranular cracking.

As for other factors which influence NC α -iron's mechanical properties, *e.g.* strain localization [78], strain rate and deformation temperature, they would be included in our follow-up studies.

4.4 Summary

In summary, we investigated the effects of annealing on the mechanical properties of NC α -iron and relevant mechanisms. The moderate annealing or recovery treatment orders defects, eliminates or minimizes the residual stress and drives GBs towards the equilibrium state. As a result, the annealing treatment not only increases the strength of the NC α -iron by reducing dislocation emission sources but also improves its ductility through strengthening the GBs' resistance to intergranular cracking. The improvement in ductility of the NC material by annealing demonstrated in this computational study is an indication that those experimental observations of annealing-induced loss of ductility in NC materials, reported in the literature, should not be an intrinsic phenomenon and could be attributed to other possible factors, such as impurity segregation or strain localization at grain boundaries. Besides, this study also indicates that annealing treatment is an essential step for obtaining a well-defined NC structure with superior mechanical properties.

5. Conclusions

5.1 Conclusions

In this work, molecular dynamics simulations are employed to investigate the 1) deformation behaviors of α -iron containing different types of grain boundary and 2) the effects of annealing treatment on mechanical properties of nanocrystalline α -iron. The following are two main conclusions drawn from this thesis study:

- 1) To investigate the deformation behavior of α -iron, a series of bicrystal model containing $\langle 110 \rangle$ tilted grain boundaries were generated and deformed. For the symmetrically tilted grain boundary (STGB), we found that the yield strength is mainly determined by Schmid factor. For the asymmetrically tilted grain boundary (ATGB), yielding behaviors are determined by local structures and local stresses in grain boundary areas.
- 2) Molecular dynamics simulation is employed to study the effects of annealing on structure and mechanical properties of cyclic deformed NC α -iron, which simulates SPD-processed α -iron. Under controllable computational conditions, external-influencing factors such as impurity segregation, surface contamination and precipitation, *etc.* can be excluded, so that one could be able to understand intrinsic effects of annealing and clarify the discrepancies in reported studies. It is demonstrated that grain boundaries in the deformed NC α -iron evolve to a more equilibrium state during annealing, eliminating or minimizing the residual stress. The equilibrated structure increases the system's strength by reducing dislocation

emission sources. The originally proposed analytical method, which could quantitatively characterize the evolution of cracks during deformations, shows annealing could improve NC α -iron's ductility through strengthening grain boundaries' resistance to intergranular cracks. The results and atomic-level analysis indicate that the annealing treatment is an essential process strategy for obtaining a well-defined NC structure with superior mechanical properties.

5.2 Future works

Due to the limited computational resource, current molecular dynamics simulations were conducted with 3D periodic conditions and relatively high strain rate. With the development of MD technique and computer science, the effects of strain localization, strain rate, deformation temperatures shall be included in the future study.

Furthermore, iron-based alloys instead of pure iron are usually applied in industry as structure materials. To expand our molecular dynamics study on pure α -iron to iron-based alloys (*e.g.* Fe-C, Fe-Ni alloys), accurate interatomic potentials are required.

Bibliography

- [1] H. Gleiter, "Nanocrystalline materials," *Prog. Mater. Sci.*, vol. 33, pp. 223–315, 1989.
- [2] B. Yu, A. Lesiuk, E. Davis, R. T. Irvin, and D. Y. Li, "Surface nanocrystallization for bacterial control," *Langmuir*, vol. 26, no. 13, pp. 10930–4, Jul. 2010.
- [3] I. P. Semenova, G. I. Raab, L. R. Saitova, and R. Z. Valiev, "The effect of equal-channel angular pressing on the structure and mechanical behavior of Ti–6Al–4V alloy," *Mater. Sci. Eng. A*, vol. 387–389, pp. 805–808, Dec. 2004.
- [4] X. Huang, N. Hansen, and N. Tsuji, "Hardening by annealing and softening by deformation in nanostructured metals," *Science*, vol. 312, no. 5771, pp. 249–51, Apr. 2006.
- [5] Y. Ivanisenko, R. Z. Valiev, and H.-J. Fecht, "Grain boundary statistics in nanostructured iron produced by high pressure torsion," *Mater. Sci. Eng. A*, vol. 390, no. 1–2, pp. 159–165, Jan. 2005.
- [6] X. Y. Wang and D. Y. Li, "Mechanical, electrochemical and tribological properties of nano-crystalline surface of 304 stainless steel," *Wear*, vol. 255, no. 7–12, pp. 836–845, Aug. 2003.
- [7] X. Y. Mao, D. Y. Li, F. Fang, R. S. Tan, and J. Q. Jiang, "A simple technique of nanocrystallizing metallic surfaces for enhanced resistances to mechanical and electrochemical attacks," *Mater. Sci. Eng. A*, vol. 527, no. 12, pp. 2875–2880, May 2010.
- [8] X. S. Guan, Z. F. Dong, and D. Y. Li, "Surface nanocrystallization by sandblasting and annealing for improved mechanical and tribological properties," *Nanotechnology*, vol. 16, no. 12, pp. 2963–2971, Dec. 2005.
- [9] X. P. Jiang, X. Y. Wang, J. X. Li, D. Y. Li, C.-S. Man, M. J. Shepard, and T. Zhai, "Enhancement of fatigue and corrosion properties of pure Ti by sandblasting," *Mater. Sci. Eng. A*, vol. 429, no. 1–2, pp. 30–35, Aug. 2006.
- [10] X. Tang and D. Y. Li, "Production of alloyed nanocrystalline surfaces by combined punching, sandblasting and recovery treatments," *Scr. Mater.*, vol. 58, no. 12, pp. 1090–1093, Jun. 2008.
- [11] E.O.Hall, "The Deformation and Ageing of Mild Steel: III Discussion of Results," *Proc. Phys. Soc.*, vol. 64, pp. 747–753, 1951.

- [12] M. A. Meyers, A. Mishra, and D. J. Benson, "Mechanical properties of nanocrystalline materials," *Prog. Mater. Sci.*, vol. 51, no. 4, pp. 427–556, May 2006.
- [13] K. Kumar, H. Van Swygenhoven, and S. Suresh, "Mechanical behavior of nanocrystalline metals and alloys," *Acta Mater.*, vol. 51, no. 19, pp. 5743–5774, Nov. 2003.
- [14] J. Schiøtz and K. W. Jacobsen, "A maximum in the strength of nanocrystalline copper," *Science*, vol. 301, no. 5638, pp. 1357–9, Sep. 2003.
- [15] R. Valiev, R. Islamgaliev, and I. Alexandrov, "Bulk nanostructured materials from severe plastic deformation," *Prog. Mater. Sci.*, vol. 45, no. 2, 2000, pp. 103–189.
- [16] Y. M. Wang, S. Cheng, Q. M. Wei, E. Ma, T. G. Nieh, and a. Hamza, "Effects of annealing and impurities on tensile properties of electrodeposited nanocrystalline Ni," *Scr. Mater.*, vol. 51, no. 11, pp. 1023–1028, Nov. 2004.
- [17] R. Valiev, A. Sergueeva, and A. K. Mukherjee, "The effect of annealing on tensile deformation behavior of nanostructured SPD titanium," *Scr. Mater.*, vol. 49, no. 7, pp. 669–674, Oct. 2003.
- [18] X. Y. Mao, D. Y. Li, F. Fang, R. S. Tan, and J. Q. Jiang, "Can severe plastic deformation alone generate a nanocrystalline structure?," *Philos. Mag. Lett.*, vol. 90, no. 5, pp. 349–360, May 2010.
- [19] B. Yu, E. M. Davis, R. S. Hodges, R. T. Irvin, and D. Y. Li, "Surface nanocrystallization of stainless steel for reduced biofilm adherence.," *Nanotechnology*, vol. 19, no. 33, p. 335101, Aug. 2008.
- [20] C. H. Moelle and H. J. Fecht, "Thermal stability of nanocrystalline iron prepared by mechanical attrition," *Nanostructured Mater.*, vol. 6, no. 95, pp. 421–424, 1995.
- [21] E. Ma, T. Shen, and X. Wu, "Nanostructured metals: Less is more," *Nat. Mater.*, vol. 5, no. July, pp. 515–516, 2006.
- [22] J. R. Greer, W. C. Oliver, and W. D. Nix, "Size dependence of mechanical properties of gold at the micron scale in the absence of strain gradients," *Acta Mater.*, vol. 53, no. 6, pp. 1821–1830, Apr. 2005.
- [23] G. J. Tucker and D. L. McDowell, "Non-equilibrium grain boundary structure and inelastic deformation using atomistic simulations," *Int. J. Plast.*, vol. 27, no. 6, pp. 841–857, Jun. 2011.
- [24] A. Hasnaoui, H. Van Swygenhoven, and P. Derlet, "On non-equilibrium grain boundaries and their effect on thermal and mechanical behaviour: a molecular

- dynamics computer simulation,” *Acta Mater.*, vol. 50, no. 15, pp. 3927–3939, Sep. 2002.
- [25] E. Ma, “Instabilities and ductility of nanocrystalline and ultrafine-grained metals,” *Scr. Mater.*, vol. 49, no. 7, pp. 663–668, Oct. 2003.
- [26] Z. X. Wu, Y. W. Zhang, M. H. Jhon, and D. J. Srolovitz, “Anatomy of nanomaterial deformation: Grain boundary sliding, plasticity and cavitation in nanocrystalline Ni,” *Acta Mater.*, vol. 61, no. 15, pp. 5807–5820, Sep. 2013.
- [27] C. Pande, R. Masumura, and R. Armstrong, “Pile-up based Hall-Petch relation for nanoscale materials,” *Nanostructured Mater.*, vol. 2, no. 9, pp. 323–331, 1993.
- [28] A. Ball and M. Hutchison, “Superplasticity in the Aluminium–Zinc eutectoid,” *Met. Sci.*, vol. 3, pp. 1–7, 1969.
- [29] D. Moldovan, D. Wolf, and S. R. Phillpot, “Theory of diffusion-accommodated grain rotation in columnar polycrystalline microstructures,” *Acta Mater.*, vol. 49, no. 17, pp. 3521–3532, Oct. 2001.
- [30] M. I. Mendeleev, H. Zhang, and D. J. Srolovitz, “Grain boundary self-diffusion in Ni: Effect of boundary inclination,” *J. Mater. Res.*, vol. 20, no. 05, pp. 1146–1153, Mar. 2005.
- [31] H. Zhang, D. J. Srolovitz, J. F. Douglas, and J. A. Warren, “Atomic motion during the migration of general [001] tilt grain boundaries in Ni,” *Acta Mater.*, vol. 55, no. 13, pp. 4527–4533, Aug. 2007.
- [32] J. Brown and Y. Mishin, “Dissociation and faceting of asymmetrical tilt grain boundaries: Molecular dynamics simulations of copper,” *Phys. Rev. B*, vol. 76, no. 13, p. 134118, Oct. 2007.
- [33] V. Randle, *The role of the coincidence site lattice in grain boundary engineering*. London: Institute of Materials, 1996, p. 128.
- [34] P. Lin, G. Palumbo, U. Erb, and K. Aust, “Influence of grain boundary character distribution on sensitization and intergranular corrosion of alloy 600,” *Scr. Metall. Mater.*, vol. 33, no. 9, pp. 1387–1392, 1995.
- [35] S. Kobayashi, T. Maruyama, S. Tsurekawa, and T. Watanabe, “Grain boundary engineering based on fractal analysis for control of segregation-induced intergranular brittle fracture in polycrystalline nickel,” *Acta Mater.*, vol. 60, no. 17, pp. 6200–6212, Oct. 2012.
- [36] E. M. Lehockey and G. Palumbo, “On the creep behaviour of grain boundary engineered nickel,” *Mater. Sci. Eng. A*, vol. 237, no. 2, pp. 168–172, Sep. 1997.

- [37] B. Alexandreanu, B. H. Sencer, V. Thaveeprungsriporn, and G. S. Was, “The effect of grain boundary character distribution on the high temperature deformation behavior of Ni–16Cr–9Fe alloys,” *Acta Mater.*, vol. 51, no. 13, pp. 3831–3848, Aug. 2003.
- [38] V. Randle, “Mechanism of twinning-induced grain boundary engineering in low stacking-fault energy materials,” *Acta Mater.*, vol. 47, no. 15–16, pp. 4187–4196, Nov. 1999.
- [39] M. Tschopp, K. Solanki, F. Gao, and X. Sun, “Probing grain boundary sink strength at the nanoscale: Energetics and length scales of vacancy and interstitial absorption by grain boundaries in α -Fe,” *Phys. Rev. B*, vol. 064108, pp. 1–21, 2012.
- [40] H. Nakashima and M. Takeuchi, “Grain boundary energy and structure of alpha-Fe< 110> symmetric tilt boundary,” *Tetsu-to-Hagane(Journal Iron Steel Inst. Japan)*, vol. 86, no. 5, pp. 357–362, 2000.
- [41] S. K. Bhattacharya, S. Tanaka, Y. Shiihara, and M. Kohyama, “Ab initio study of symmetrical tilt grain boundaries in bcc Fe: structural units, magnetic moments, interfacial bonding, local energy and local stress.,” *J. Phys. Condens. Matter*, vol. 25, no. 13, p. 135004, Apr. 2013.
- [42] D. Terentyev and F. Gao, “Blunting of a brittle crack at grain boundaries: An atomistic study in BCC Iron,” *Mater. Sci. Eng. A*, vol. 576, pp. 231–238, Aug. 2013.
- [43] D. Spearot, M. Tschopp, K. Jacob, and D. McDowell, “Tensile strength of {100} and {110} tilt bicrystal copper interfaces,” *Acta Mater.*, vol. 55, no. 2, pp. 705–714, Jan. 2007.
- [44] S. B. Lee, J.-H. Lee, Y.-H. Cho, D.-Y. Kim, W. Sigle, F. Phillipp, and P. a. van Aken, “Grain-boundary plane orientation dependence of electrical barriers at $\Sigma 5$ boundaries in SrTiO₃,” *Acta Mater.*, vol. 56, no. 18, pp. 4993–4997, Oct. 2008.
- [45] M. P. Allen and D. J. Tildesley, *Computer Simulation of Liquids*, vol. 42, no. 3. Oxford: Oxford Science Publications, 1987, p. 385.
- [46] J. E. Jones, “On the Determination of Molecular Fields. II. From the Equation of State of a Gas,” *Proc. R. Soc. A Math. Phys. Eng. Sci.*, vol. 106, no. 738, pp. 463–477, Oct. 1924.
- [47] M. Daw and M. Baskes, “Embedded-atom method: Derivation and application to impurities, surfaces, and other defects in metals,” *Phys. Rev. B*, vol. 29, no. 12, pp. 6443–6453, Jun. 1984.

- [48] M. I. Mendeleev, S. Han, D. J. Srolovitz, G. J. Ackland, D. Y. Sun, and M. Asta, “Development of new interatomic potentials appropriate for crystalline and liquid iron,” *Philos. Mag.*, vol. 83, no. 35, pp. 3977–3994, Dec. 2003.
- [49] D. Terentyev, X. He, a. Serra, and J. Kuriplach, “Structure and strength of $\langle 110 \rangle$ tilt grain boundaries in bcc Fe: An atomistic study,” *Comput. Mater. Sci.*, vol. 49, no. 2, pp. 419–429, Aug. 2010.
- [50] S. Li, X. Ding, J. Deng, T. Lookman, J. Li, X. Ren, J. Sun, and A. Saxena, “Superelasticity in bcc nanowires by a reversible twinning mechanism,” *Phys. Rev. B*, vol. 82, no. 20, p. 205435, Nov. 2010.
- [51] I. Ringdalen Vatne, A. Stukowski, C. Thaulow, E. Østby, and J. Marian, “Three-dimensional crack initiation mechanisms in bcc-Fe under loading modes I, II and III,” *Mater. Sci. Eng. A*, vol. 560, pp. 306–314, Jan. 2013.
- [52] A. P. Gerlich, L. Yue, P. F. Mendez, and H. Zhang, “Plastic deformation of nanocrystalline aluminum at high temperatures and strain rate,” *Acta Mater.*, vol. 58, no. 6, pp. 2176–2185, Apr. 2010.
- [53] X. Li, Y. Wei, L. Lu, K. Lu, and H. Gao, “Dislocation nucleation governed softening and maximum strength in nano-twinned metals,” *Nature*, vol. 464, no. 7290, pp. 877–80, May 2010.
- [54] G. Voronoï, “Nouvelles applications des paramètres continus à la théorie des formes quadratiques. Deuxième mémoire. Recherches sur les paralléloèdres primitifs,” *J. für die reine und Angew. Math.*, vol. 134, pp. 97–102, 1908.
- [55] H. Tsuzuki, P. S. Branicio, and J. P. Rino, “Structural characterization of deformed crystals by analysis of common atomic neighborhood,” *Comput. Phys. Commun.*, vol. 177, no. 6, pp. 518–523, Sep. 2007.
- [56] A. Stukowski and K. Albe, “Dislocation detection algorithm for atomistic simulations,” *Model. Simul. Mater. Sci. Eng.*, vol. 18, no. 2, p. 025016, Mar. 2010.
- [57] S. Nosé, “A unified formulation of the constant temperature molecular dynamics methods,” *J. Chem. Phys.*, 1984.
- [58] W. Hoover, “Canonical dynamics: Equilibrium phase-space distributions,” *Phys. Rev. A*, vol. 31, no. 3, pp. 1695–1697, 1985.
- [59] S. Plimpton, “Fast parallel algorithms for short-range molecular dynamics,” *J. Comput. Phys.*, vol. 117, no. June 1994, pp. 1–42, 1995.
- [60] J. Li, “AtomEye: an efficient atomistic configuration viewer,” *Model. Simul. Mater. Sci. Eng.*, vol. 0393, no. 03, pp. 173–177, 2003.

- [61] D. Faken and H. Jónsson, “Systematic analysis of local atomic structure combined with 3D computer graphics,” *Comput. Mater. Sci.*, 1994.
- [62] C. H. Rycroft, “VORO++: a three-dimensional voronoi cell library in C++,” *Chaos*, vol. 19, no. 4, p. 041111, Dec. 2009.
- [63] N. Gao, C.-C. Fu, M. Samaras, R. Schäublin, M. Victoria, and W. Hoffelner, “Multiscale modelling of bi-crystal grain boundaries in bcc iron,” *J. Nucl. Mater.*, vol. 385, no. 2, pp. 262–267, Mar. 2009.
- [64] F. Sorbello, P. E. J. Flewitt, G. Smith, and a. G. Crocker, “The role of deformation twins in brittle crack propagation in iron–silicon steel,” *Acta Mater.*, vol. 57, no. 9, pp. 2646–2656, May 2009.
- [65] D. Farkas, “Twinning and recrystallisation as crack tip deformation mechanisms during fracture,” *Philos. Mag.*, vol. 85, no. 2–3, pp. 387–397, Jan. 2005.
- [66] T. Šmida and J. Bošanský, “Deformation twinning and its possible influence on the ductile brittle transition temperature of ferritic steels,” *Mater. Sci. Eng. A*, vol. 287, no. 1, pp. 107–115, Jul. 2000.
- [67] M. D. Sangid, T. Ezaz, H. Sehitoglu, and I. M. Robertson, “Energy of slip transmission and nucleation at grain boundaries,” *Acta Mater.*, vol. 59, no. 1, pp. 283–296, Jan. 2011.
- [68] P. M. Derlet, H. Van Swygenhoven†, and a. Hasnaoui, “Atomistic simulation of dislocation emission in nanosized grain boundaries,” *Philos. Mag.*, vol. 83, no. 31–34, pp. 3569–3575, Oct. 2003.
- [69] A. Stukowski, “Visualization and analysis of atomistic simulation data with OVITO—the Open Visualization Tool,” *Model. Simul. Mater. Sci. Eng.*, vol. 18, no. 1, p. 015012, Jan. 2010.
- [70] X. Tong, H. Zhang, and D. Y. Li, “Effects of misorientation and inclination on mechanical response of <110> tilt grain boundaries in alpha-Fe to external stresses,” *Model. Simul. Mater. Sci. Eng.*, vol. 22, p. 065016, 2014.
- [71] P. M. Derlet, H. Van Swygenhoven, and A. Hasnaoui, “Atomistic simulation of dislocation emission in nanosized grain boundaries,” *Philos. Mag.*, vol. 83, no. 31–34, pp. 3569–3575, Oct. 2003.
- [72] X. W. Gu, Z. Wu, Y.-W. Zhang, D. J. Srolovitz, and J. R. Greer, “Microstructure versus flaw: mechanisms of failure and strength in nanostructures,” *Nano Lett.*, vol. 13, no. 11, pp. 5703–9, Nov. 2013.

- [73] S. L. Frederiksen, K. W. Jacobsen, and J. Schiøtz, "Simulations of intergranular fracture in nanocrystalline molybdenum," *Acta Mater.*, vol. 52, no. 17, pp. 5019–5029, Oct. 2004.
- [74] D. Farkas, H. Van Swygenhoven, and P. Derlet, "Intergranular fracture in nanocrystalline metals," *Phys. Rev. B*, vol. 66, no. 6, p. 060101, Aug. 2002.
- [75] J. Schiøtz, F. Di Tolla, and K. Jacobsen, "Softening of nanocrystalline metals at very small grain sizes," *Nature*, vol. 391, no. February, pp. 561–563, 1998.
- [76] V. Yamakov, D. Wolf, S. Phillpot, and H. Gleiter, "Deformation twinning in nanocrystalline Al by molecular-dynamics simulation," *Acta Mater.*, vol. 50, pp. 5005–5020, 2002.
- [77] D. H. Warner, W. A. Curtin, and S. Qu, "Rate dependence of crack-tip processes predicts twinning trends in f.c.c. metals," *Nat. Mater.*, vol. 6, no. 11, pp. 876–81, Nov. 2007.
- [78] Q. Wei, D. Jia, K. T. Ramesh, and E. Ma, "Evolution and microstructure of shear bands in nanostructured Fe," *Appl. Phys. Lett.*, vol. 81, no. 7, p. 1240, 2002.